

**AFRL-PR-WP-TR-2002-2002**

**SCIENTIFIC RESEARCH IN AIRCRAFT  
MECHANICAL/THERMAL  
TECHNOLOGY**



**DR. SCOTT K. THOMAS  
TRAVIS E. MICHALAK  
JOEL T. LAUER  
DR. KIRK L. YERKES**

**WRIGHT STATE UNIVERSITY  
DEPARTMENT OF MECHANICAL AND MATERIALS ENGINEERING  
DAYTON, OH 45435-0001**

**NOVEMBER 2001**

**INTERIM REPORT FOR PERIOD 21 AUGUST 2000 – 20 AUGUST 2001**

**Approved for public release; distribution unlimited**

**20020402 137**

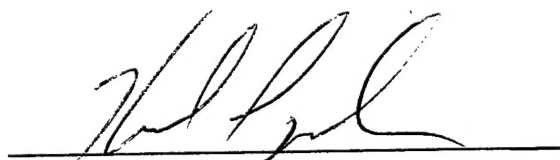
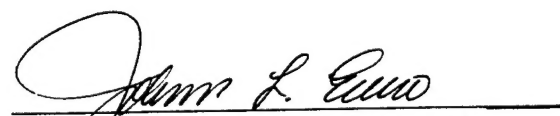
**PROPULSION DIRECTORATE  
AIR FORCE RESEARCH LABORATORY  
AIR FORCE MATERIEL COMMAND  
WRIGHT-PATTERSON AIR FORCE BASE, OH 45433-7251**

## NOTICE

Using government drawings, specifications, or other data included in this document for any purpose other than government procurement does not in any way obligate the U.S. Government. The fact that the government formulated or supplied the drawings, specifications, or other data does not license the holder or any other person or corporation; or convey and rights or permission to manufacture, use, or sell any patented invention that may relate to them.

This report has been reviewed by the Office of Public Affairs (ASC/PA) and is releasable to the National Technical Information Service (NTIS). At NTIS, it will be available to the general public, including foreign nations.

This technical report has been reviewed and is approved for publication.

  
KIRK L. YERKES  
Project Engineer  
Power Division  
BRIAN G. HAGER  
Chief, Energy Storage & Thermal Sciences Branch  
Power Division  
JOANN L. ERNO, Lt Colonel, USAF  
Deputy Chief  
Power Division

Copies of this report should not be returned unless return is required by security considerations, contractual obligations, or notice on a specific document.

**REPORT DOCUMENTATION PAGE***Form Approved*  
*OMB No. 074-0188*

Public reporting burden for this collection of information is estimated to average 1 hour per response, including the time for reviewing instructions, searching existing data sources, gathering and maintaining the data needed, and completing and reviewing this collection of information. Send comments regarding this burden estimate or any other aspect of this collection of information, including suggestions for reducing this burden to Washington Headquarters Services, Directorate for Information Operations and Reports, 1215 Jefferson Davis Highway, Suite 1204, Arlington, VA 22202-4302, and to the Office of Management and Budget, Paperwork Reduction Project (0704-0188), Washington, DC 20503

<b>1. AGENCY USE ONLY (Leave blank)</b>		<b>2. REPORT DATE</b> NOVEMBER 2001		<b>3. REPORT TYPE AND DATES COVERED</b> Interim, 08/21/2000 – 08/20/2001	
<b>4. TITLE AND SUBTITLE</b>  SCIENTIFIC RESEARCH IN AIRCRAFT MECHANICAL/THERMAL TECHNOLOGY				<b>5. FUNDING NUMBERS</b>  C: F33615-98-1-2844 PE: 62203 PN: 3145 TN: 20 WU: C5	
<b>6. AUTHOR(S)</b> DR. SCOTT K. THOMAS, TRAVIS E. MICHALAK, JOEL T. LAUER, and DR. KIRK L. YERKES					
<b>7. PERFORMING ORGANIZATION NAME(S) AND ADDRESS(ES)</b>  WRIGHT STATE UNIVERSITY DEPARTMENT OF MECHANICAL AND MATERIALS ENGINEERING DAYTON, OH 45435-0001				<b>8. PERFORMING ORGANIZATION REPORT NUMBER</b>	
<b>9. SPONSORING / MONITORING AGENCY NAME(S) AND ADDRESS(ES)</b>  PROPULSION DIRECTORATE AIR FORCE RESEARCH LABORATORY AIR FORCE MATERIEL COMMAND WRIGHT-PATTERSON AIR FORCE BASE, OH 45433-7251 POC: Kirk Yerkes, AFRL/PRPS, (937) 255-5721				<b>10. SPONSORING / MONITORING AGENCY REPORT NUMBER</b>  AFRL-PR-WP-TR-2002-2002	
<b>11. SUPPLEMENTARY NOTES:</b>					
<b>12a. DISTRIBUTION / AVAILABILITY STATEMENT</b> Approved for public release; distribution unlimited.					<b>12b. DISTRIBUTION CODE</b>
<b>13. ABSTRACT (Maximum 200 Words)</b> This interim report describes the progress to date on three individual projects. The project entitled, "Micro Capillary Pumped Loop Testing" deals with the design, manufacture and calibration of an experimental facility for testing capillary pumped loops embedded in silicon wafers. A description of the current experimental setup and the details of the calibration of the laser controller and the calibration of the thermocouples are provided. The second project is entitled, "Design and Testing of a Thermodynamic Filling Station for Miniature Heat Pipes," which concerns a novel filling procedure for miniature heat pipes. The experimental setup and procedure is described, which involves a vacuum chamber within an environmental chamber. A thermodynamic analysis of the process is provided, and the results are compared to the experimental data. The final project of this interim report is entitled, "Acceleration Testing of Three Raytheon Heat Pipes using the AFRL/PRPS Centrifuge Table." The objective of this project was to determine the performance of heat pipes under various acceleration conditions, which were imposed by the centrifuge table located in Bldg. 71-B H-Bay in Area B of Wright-Patterson AFB. Information on the experimental setup, experimental procedure, and an analysis of the results are provided.					
<b>14. SUBJECT TERMS</b> Micro capillary pumped loop, heat pipe fill station, centrifugal testing					<b>15. NUMBER OF PAGES</b> 64
					<b>16. PRICE CODE</b>
<b>17. SECURITY CLASSIFICATION OF REPORT</b> Unclassified	<b>18. SECURITY CLASSIFICATION OF THIS PAGE</b> Unclassified	<b>19. SECURITY CLASSIFICATION OF ABSTRACT</b> Unclassified		<b>20. LIMITATION OF ABSTRACT</b> SAR	
NSN 7540-01-280-5500				Standard Form 298 (Rev. 2-89) Prescribed by ANSI Std. Z39-18 298-102	

## Contents

<b>1</b>	<b>Micro Capillary Pumped Loop Testing</b>	<b>1</b>
1.1	Abstract . . . . .	1
1.2	Experimental Setup . . . . .	1
1.2.1	Calibration . . . . .	4
1.2.2	Uncertainty Analysis . . . . .	8
1.3	Summary and Future Work . . . . .	9
1.4	Nomenclature . . . . .	22
<b>2</b>	<b>Design and Testing of a Thermodynamic Filling Station for Miniature Heat Pipes</b>	<b>23</b>
2.1	Abstract . . . . .	23
2.2	Introduction . . . . .	23
2.3	Analytical Model . . . . .	25
2.4	Experimental Setup . . . . .	27
2.5	Results and Discussion . . . . .	28
2.6	Conclusions and Future Directions . . . . .	29
2.7	References . . . . .	29
2.8	Nomenclature . . . . .	29
<b>3</b>	<b>Acceleration Testing of Three Raytheon Heat Pipes using the AFRL/PRPS Centrifuge Table</b>	<b>36</b>
3.1	Abstract . . . . .	36
3.2	Experimental Setup . . . . .	36
3.3	Experimental Procedure . . . . .	38
3.4	Results and Discussion . . . . .	40
3.5	Conclusions . . . . .	42

## List of Figures

1	Variations of the basic $\mu$ CPL design. . . . .	11
---	---	----

2	Schematic of $\mu$ -CPL test setup. . . . .	12
3	Mounting fixture for the $\mu$ CPL. . . . .	13
4	Photograph of the copper calorimeter. . . . .	14
5	Photograph showing thermocouples adhered to the back of the $\mu$ CPL wafer with vacuum epoxy. The stainless steel fill tube is on the left-hand side. . . .	15
6	CO <sub>2</sub> laser calibration: (a) Typical calorimeter temperature increase trace (LCS = 10%); (b) Typical laser power measurement traces (LCS = 10%); (c) Heat rates versus LCS (Data points in square brackets were taken when the borosilicate glass melted on the wafer). . . . .	16
7	Temperature responses of a typical thermocouple, the resistance temperature detector, and the recirculating chiller bath. . . . .	17
8	Temperature reading obtained during calibration (Thermocouple 201): (a) Temperature obtained by RTD vs. temperature reading from TC201; (b) Error obtained when substituting raw data into the linear best-fit equation for TC201. . . . .	18
9	Schematic of the heat pipe filling station: (a) Current system; (b) System incorporating a standard filling station. . . . .	32
10	Thermodynamic heat pipe filling station. . . . .	33
11	Critical orifice plate: (a) Internal design; (b) Installation in the filling station. . . . .	34
12	Mass of liquid in the heat pipe at State 2 versus initial liquid charge ( $m_{a, hp} = 0$ , $P_{vc,1} = 30$ mTorr, $T_1 = 25^\circ\text{C}$ , $P_{atm} = 10^5$ Pa). . . . .	35
13	Close-up view of the heat pipe assembly mounted to the centrifuge table. . . . .	44
14	Placement of the heat pipe assembly on the centrifuge table ( $R = 44.5$ inches). . . . .	45
15	Typical start-up test results for $a_r = 5.0\text{-g}$ : (a) 3IHP (RAY33); (b) 6IHP (RAY22); (c) 9IHP (RAY9). . . . .	46
16	Temperature differences between the evaporator and adiabatic sections for the start-up tests. . . . .	47
17	Typical burst test results for $a_r = 5.0\text{-g}$ : (a) 3IHP (RAY28); (b) 6IHP (RAY16); (c) 6IHP (RAY17); (d) 9IHP (RAY2). . . . .	48

18	Temperature differences between the evaporator and adiabatic sections for the burst tests. . . . .	49
19	Start-up response characteristics. . . . .	50

## List of Tables

1	Laser calibration data. . . . .	19
2	Laser calibration data, continued. . . . .	20
3	Laser calibration data, continued. . . . .	21
4	Thermocouple calibration equations: $T_{\text{actual}} = mT_{\text{reading}} + b$ (Valid ranges: TCs 201–210, $10^{\circ}\text{C} \leq T_{\text{reading}} \leq 95^{\circ}\text{C}$ ; TCs 211 and 212, $10^{\circ}\text{C} \leq T_{\text{reading}} \leq 40^{\circ}\text{C}$ ). . . . .	22
5	Heat pipe filling station volume data ( $V_{vc} = 514.3 \text{ in}^3 = 8.428 \times 10^{-3} \text{ m}^3$ , $V_m = 1.591 \text{ in}^3 = 2.607 \times 10^{-5} \text{ m}^3$ , $V_{hp} = 0.047 \text{ in}^3 = 7.702 \times 10^{-7} \text{ m}^3$ , $V_t = 8.455 \times 10^{-3} \text{ m}^3$ ). . . . .	37
6	Temperature differences between the evaporator and adiabatic sections for the start-up tests (Fig. 16). . . . .	51
7	Temperature differences between the evaporator and adiabatic sections for the burst tests (Fig. 18). . . . .	52
8	Start-up response characteristics (Fig. 19). . . . .	53

# 1 Micro Capillary Pumped Loop Testing

## 1.1 Abstract

This project seeks to determine the operational characteristics of a micro-capillary pumped loop. This thermal management device is to be directly integrated into the silicon chips used in various devices. An experimental testbed has been constructed and calibrated while the test specimens were being manufactured. This chapter provides details concerning the experimental setup and preliminary calibration information, which will be used in the near future when a fully instrumented micro-capillary pumped loop will be tested.

## 1.2 Experimental Setup

The objective of these experiments was to determine the heat transfer capabilities of micro-Capillary Pumped Loops ( $\mu$ CPLs) which are formed using a layer of borosilicate glass anodically bonded to a silicon wafer. These  $\mu$ CPLs are being tested to determine their suitability for the thermal management of microprocessors.

Figure 1 shows two typical  $\mu$ CPL designs. Several  $\mu$ CPLs were manufactured on a 3.9-inch dia. silicon wafer at the University of California at Berkeley using photolithographic techniques. The individual  $\mu$ CPLs were cut from the wafer using a diamond saw on a mini vertical mill. The  $\mu$ CPLs consisted of a series of channels etched in the silicon wafer. These channels made up part of the evaporator section, the condenser section, and the interconnecting vapor and liquid lines. In addition, a hole was etched completely through the silicon to allow the installation of a fill tube, which would in turn be attached to a remote working fluid reservoir. A thin sheet of borosilicate glass was bonded to the front of the silicon. This glass had grooves etched into the sections that were positioned over the evaporator and condenser sections of the  $\mu$ CPL. These grooves acted as a wick structure and provided the capillary pressure that was required for circulation of the working fluid. In an actual application, the glass would be replaced by another sheet of silicon, but for experimental purposes, glass was used to allow observation of the working fluid while the  $\mu$ CPL was being tested. Another reason that glass was used was that, while silicon is virtually transparent to the CO<sub>2</sub> laser energy, the borosilicate glass absorbed a significant

portion of the incident laser light. This heated the glass and provided the source of thermal energy needed for testing the  $\mu$ CPLs.

Figure 2 shows an overall schematic diagram of the experimental setup. This setup provided a means to input heat to the  $\mu$ CPL evaporator section using a laser, extract heat from the condenser section using a calorimeter, insulate the  $\mu$ CPL from parasitic heat losses, and record temperature data. In addition, photographic records of the tests could be collected.

The  $\mu$ CPL wafer was enclosed in a stainless steel vacuum chamber to reduce natural convective heat losses from the surface. The chamber could be evacuated to a pressure of less than  $10^{-3}$  Torr (Varian Turbo-V450 vacuum pump), which was measured using a thermocouple gauge and a more accurate ionization gauge (Varian Model 0571-K2471-303). In addition, multi-layer mylar radiation insulation was installed on the interior of the vacuum chamber to reduce thermal radiation heat transfer. The  $\mu$ CPL was isolated from conductive heat transfer by using an acrylic holding fixture, as shown in Fig. 3. Grooves were machined in the upper and lower acrylic fixtures to hold the  $\mu$ CPL. The fixtures were in turn mounted to an aluminum ring, which was held in the chuck of a micrometer stage. This stage could rotate the aluminum ring, as well as move it horizontally and vertically, to position the  $\mu$ CPL in front of the ZnSe window in the end of the vacuum chamber.

Heat was applied to the  $\mu$ CPL evaporator section by a 25-Watt CO<sub>2</sub> laser (Synrad Model J48-2W). Since the wavelength of this laser ( $10.5\ \mu\text{m}$ ) is not in the visible range, a Helium-Neon laser (Uniphase Novette 1508-0) was used to determine the location of the CO<sub>2</sub> laser spot. Alignment was verified by placing a piece of paper in front of the vacuum chamber and burning it slightly with the CO<sub>2</sub> laser. After the CO<sub>2</sub> laser was deactivated, the removable mirror M1 (Fig. 2) was then installed, and the HeNe was activated. The HeNe laser beam was then aligned with the burn spot using adjusting screws on the removable mirror. Once the two beams were aligned, changing the angle of the turning mirror M2 would redirect both laser beams. In this way, the CO<sub>2</sub> laser beam could be aimed onto the  $\mu$ CPL evaporator using the HeNe and the adjusting screws on the turning mirror M2. The CO<sub>2</sub> laser beam was turned, focused with a plano-convex lens (ZnSe, 1.5 inch dia., 30 ft focal length, AR coated for  $9.2 - 10.6\ \mu\text{m}$ ), and passed through a window (ZnSe, AR coated for  $9.2 - 10.6\ \mu\text{m}$ ) into the vacuum chamber. The focusing lens provided a means to control the diameter



of the beam at the surface of the test specimen, and therefore the heat flux applied to the evaporator of the  $\mu$ CPL. The CO<sub>2</sub> laser beam was directed through a length of PVC pipe to reduce the possibility of foreign objects accidentally being placed in the path of the invisible beam, which would have caused a hazardous situation. There were also beam stops made of plexiglas, which is opaque to CO<sub>2</sub> laser light, along the sides of the beam path.

A water-cooled calorimeter was designed and manufactured to determine the heat rate transported by the  $\mu$ CPL (Fig. 4). It consisted of a small block of copper with stainless steel tubing silver-soldered into holes which had been drilled into one face of the block. A hole was drilled into another face of the block, which simultaneously opened both tubes. This face was then adhered to the  $\mu$ CPL using RTV sealant such that the coolant was in direct contact with the glass or silicon. The vacuum chamber had pass-through fittings to allow the coolant to flow to and from the calorimeter. Tygon tubing was used in the interior of the vacuum chamber to connect the calorimeter to the pass-through fittings. Type E thermocouples were placed in the coolant inlet and outlet lines within the vacuum chamber as close to the calorimeter as was practical. In this way, convective and conductive heat losses from the tygon tubing and along the length of the thermocouple wires to the ambient were mitigated. As shown in Fig. 2, an open reservoir was used to deliver coolant (water) at a constant mass flow rate to the calorimeter. The coolant line from the reservoir to the calorimeter was heavily insulated to reduce temperature swings when the room air conditioner cycled on and off. The mass flow rate of the water flowing through the calorimeter was calculated using a stopwatch and a Mettler scale (Model PC 4400).

Three electrical feedthroughs were mounted on the top of the chamber. One feedthrough supplied electrical power to the interior of the chamber. The other two were five-pair, Type E (Chromel/Constantan) thermocouple feedthroughs. The thermocouples that were used to make temperature measurements directly on the different points of the  $\mu$ CPL were attached to the backside of the silicon using Kapton Tape or vacuum epoxy, as shown in Fig. 5.

A digital-capable video camera (Panasonic GP-KR222) with a long-range microscope lens and a monitor with a VCR were used to observe the  $\mu$ CPLs while they were being tested. The camera was suspended just above the path of the CO<sub>2</sub> laser beam to reduce parallax. Image- and video-capturing software was used to store pictures and videos directly to a PC

during transient events such as start-up, boiling and dry-out.

### 1.2.1 Calibration

In order to accurately test the  $\mu$ CPLs, the amount of laser power delivered to the wafer had to be quantified. The thermocouples used for sensing the temperature of the wafer and the coolant inlet and outlet had to be calibrated. This section gives a detailed description of the procedures used to achieve these calibrations.

#### Laser Controller Calibration

The CO<sub>2</sub> laser beam was attenuated and partially reflected as it passed through the vacuum chamber window, and partially reflected when it struck the  $\mu$ CPL wafer. Therefore, it was necessary to calibrate to determine the above-mentioned losses. Power measurements were taken in front of and behind the vacuum chamber window. This provided a measure of the amount of attenuation/reflection caused by the window. The power output of the laser was measured by a calibrated optical power meter/disk thermopile combination (Newport Models 1815-C and 818T-10). A small blank wafer of the glass/silicon sandwich, instrumented with a water-cooled calorimeter inside the evacuated chamber, was used to determine the amount of power actually absorbed by the wafer. The amount of laser power incident on the window and the wafer, as well as the amount of power extracted by the calorimeter, were calibrated to the laser controller setting (LCS), which was in terms of the percentage of the full power output of the laser. In a preliminary setup, a ZnSe beam splitter was used with the power meter to directly measure the laser power output. However, it was determined that this arrangement caused the amount of laser power delivered to the wafer to fluctuate significantly, due to the dependence of the reflectivity of the beam splitter on the wavelength of the laser. Line hopping, or the variation of the wavelength of the CO<sub>2</sub> laser with respect to time, could not be avoided, so the beam splitter was removed from the system.

The following procedure was used to obtain the power readings in front of and behind the chamber:

1. Turn on the recirculating chiller, external pump and power supply for the CO<sub>2</sub> laser.

2. Using the HeNe laser, position the power meter in front of the chamber ("fore" position).
3. Remove the M1 mirror from the kinematic mount.
4. Set the laser controller setting to 1.0%.
5. Turn on the CO<sub>2</sub> laser.
6. After a short warm-up period, collect 500 data points using the power meter in front of the chamber.
7. Interrupt the beam with the laser aperture shutter on top of the laser.
8. Place the power meter behind the chamber ("aft" position).
9. Open the shutter on the laser.
10. Collect 500 data points using the power meter behind the chamber.
11. Using this method, alternate between the fore and aft positions until four calibration points (500 data points each) have been collected both in front of and behind the chamber.
12. Repeat steps 4 through 11, incrementing up through the desired controller settings.
13. Using the same procedure, start at the maximum LCS value and work back down through the specified settings. This will produce eight calibration points at each location (fore and aft) for each laser controller setting.

The procedure for determining the amount of power extracted by the water-cooled calorimeter on the blank wafer is as follows:

1. Turn on the recirculating chiller, external pump and power supply for the CO<sub>2</sub> laser.
2. Position the power meter in front of the vacuum chamber to validate the laser power setting.

3. Set the laser controller setting to 1.0%.
4. Turn on the CO<sub>2</sub> laser.
5. After a short warm-up period, collect 500 data points using the power meter in front of the chamber.
6. Interrupt the beam with the laser aperture shutter on top of the laser.
7. Remove the power meter.
8. Start the coolant flow rate to the calorimeter.
9. Open the shutter on the laser.
10. Adjust the coolant flow rate so the temperature increase across the calorimeter is approximately 2°C.
11. Allow the calorimeter temperatures to reach steady state (approximately 30 min.).
12. Take 8 sets of 600 data points for the calorimeter inlet and outlet temperatures. For each set, measure the mass flow rate through the calorimeter.
13. Reinstall the power meter in front of the vacuum chamber and collect 500 data points for the laser power at that location.
14. Repeat steps 3 through 13, incrementing up through the desired controller settings.

Figures 6(a) and 6(b) show typical traces obtained during calibration for the calorimeter temperature difference and the laser power versus time, respectively. In addition, Fig. 6(c) shows the results of the calibration with respect to the laser controller setting. It should be noted that the borosilicate glass melted at LCS = 30%, as indicated by the brackets surrounding this data. Tables 1—3 provide the actual values presented in Fig. 6(c). The linear best-fit equations for the data in Fig. 6(c) are as follows:

$$\dot{Q}_{\text{window}} = 0.2874 * \text{LCS} \quad (R^2 = 0.9997) \quad (1)$$

$$\dot{Q}_{\text{in}} = 0.2581 * \text{LCS} \quad (R^2 = 0.9992) \quad (2)$$

$$\dot{Q}_{\text{out}} = 0.2011 * \text{LCS} \quad (R^2 = 0.9974) \quad (3)$$

The linear equation for the power absorbed by the wafer does not include the data at LCS = 30%. In comparing eqns. (2) and (3), the amount of incident laser power absorbed by the borosilicate glass is approximately 78%.

### Thermocouple Calibration

The thermocouples used for wall temperature measurements and calorimetry were calibrated using a recirculating chiller (Lauda Model RC20) with a serial interface (Lauda Model R61) and an RTD (Hart Scientific model 5691). The working bath of the chiller was filled with PAO oil to allow for more stable temperatures. In the bath, there was a length of copper pipe with a flat sheet of copper silver-soldered over one end. Copper was chosen for its high thermal conductivity. This sheet of copper acted as a cap and a base. The other end of the copper pipe was left open. This allowed it to be filled with water and immersed in the oil bath, keeping the open end of the tube above the surface of the oil. The RTD and thermocouples were placed in the water in this copper tube, to protect them from the oil in the bath. The thermocouples were attached to the RTD, and the RTD was supported using a lab clamp to insure that it did not contact the sides or the base of the copper tube. The target temperature of the bath was set by a PC, which also read the RTD temperature and received information on the thermocouple temperatures from a data acquisition unit (Hewlett Packard Model HP34970A). The data acquisition and temperature settings were controlled by an Excel/Visual Basic for Applications program. A test program was written to determine the length of time necessary for the RTD and thermocouple readings inside the water-filled copper tube to reach steady state. The temperature of the bath was set to 38°C, and allowed to stabilize for 30 min. The program then set the target bath temperature to 40°C, and began taking data from the bath temperature sensor, the RTD, and a thermocouple. Scans were recorded continuously for approximately 2 hr as shown in Fig. 7. It was determined that the readings of the RTD and the thermocouple in the water reached steady state after approximately 30 min.

After the time taken to reach steady state was known, the actual calibration tests could be performed. A new program was written which initially set the bath temperature to 10°C, waited for 60 min., and then took 100 data points of 5 scans each. The 60-min. interval was

decided on because it should have given more than enough time for the readings to reach steady state. The program then incremented the temperature to 15°C, waited one hr, and recorded data again. It continued in this manner from 10°C to 95°C, in 5°C increments. After it had been set at 95°C for one hr and had taken the data for that temperature, it then went down to 92.5°C. From there, it went down in the same manner (5°C intervals with 60-min. time intervals) to 12.5°C. When the program was finished, there were 500 data points for each temperature from 10°C to 95°C in increments of 2.5°C. This raw data was used to determine the calibration curves for the twelve thermocouples. The temperature reading of each thermocouple was plotted against the reading of the RTD. A linear best-fit line was determined in the form  $T_{\text{actual}} = mT_{\text{reading}} + b$ , as shown in Fig. 8(a). Next, all of the temperature measurements for a specific thermocouple were evaluated by its respective best-fit equation. The difference between the value from the equation and the corresponding RTD value was calculated as shown in Fig. 8(b). This difference plus the stated NIST-traceable uncertainty of the RTD ( $\pm 0.005^\circ\text{C}$ ) was the final uncertainty for any subsequent temperature measurements for a given thermocouple (Table 4). Thermocouples 211 and 212 were used in the calorimeter. Since the coolant temperature was not anticipated to rise above 40°C, only the calibration data between 10°C and 40°C were used when calibrating these two thermocouples. There were some outlying data points that were disregarded when reporting the maximum errors in Table 4. There were no more than 10 out of 3500 of these points dropped from each graph.

### 1.2.2 Uncertainty Analysis

The formula used for finding the mass flow rate of coolant flowing through the calorimeter is

$$\dot{m} = \frac{m}{t} \quad (4)$$

The root-sum-square uncertainty for the mass flow rate is

$$\begin{aligned} \Delta \dot{m} &= \sqrt{\left(\frac{\partial \dot{m}}{\partial m} \Delta m\right)^2 + \left(\frac{\partial \dot{m}}{\partial t} \Delta t\right)^2} \\ &= \sqrt{\left(\frac{1}{t} \Delta m\right)^2 + \left(\frac{-m}{t^2} \Delta t\right)^2} \end{aligned} \quad (5)$$

The amount of heat removed from the  $\mu\text{CPL}$  by the calorimeter can be expressed by

$$\dot{Q}_{\text{out}} = \dot{m}C_p (T_{\text{out}} - T_{\text{in}}) \quad (6)$$

The uncertainty for values found using this equation is

$$\begin{aligned} \Delta\dot{Q}_{\text{out}} &= \sqrt{\left(\frac{\partial\dot{Q}_{\text{out}}}{\partial\dot{m}}\Delta\dot{m}\right)^2 + \left(\frac{\partial\dot{Q}_{\text{out}}}{\partial C_p}\Delta C_p\right)^2 + \left(\frac{\partial\dot{Q}_{\text{out}}}{\partial T_{\text{out}}}\Delta T_{\text{out}}\right)^2 + \left(\frac{\partial\dot{Q}_{\text{out}}}{\partial T_{\text{in}}}\Delta T_{\text{in}}\right)^2} \\ &= \sqrt{[C_p (T_{\text{out}} - T_{\text{in}}) \Delta\dot{m}]^2 + [\dot{m} (T_{\text{out}} - T_{\text{in}}) \Delta C_p]^2 + (\dot{m}C_p \Delta T_{\text{out}})^2 + (\dot{m}C_p \Delta T_{\text{in}})^2} \end{aligned} \quad (7)$$

The thermal resistances based on incident laser power and power extracted by the calorimeter, respectively, are

$$R_{\text{th},\text{in}} = \frac{(T_{\text{v},\text{e}} - T_{\text{v},\text{c}})}{\dot{Q}_{\text{in}}} \quad (8)$$

$$R_{\text{th},\text{out}} = \frac{(T_{\text{v},\text{e}} - T_{\text{v},\text{c}})}{\dot{Q}_{\text{out}}} \quad (9)$$

The uncertainties for these thermal resistance equations are

$$\begin{aligned} \Delta R_{\text{th},\text{in}} &= \sqrt{\left(\frac{\partial R_{\text{th},\text{in}}}{\partial T_{\text{v},\text{e}}}\Delta T_{\text{v},\text{e}}\right)^2 + \left(\frac{\partial R_{\text{th},\text{in}}}{\partial T_{\text{v},\text{c}}}\Delta T_{\text{v},\text{c}}\right)^2 + \left(\frac{\partial R_{\text{th},\text{in}}}{\partial \dot{Q}_{\text{in}}}\Delta \dot{Q}_{\text{in}}\right)^2} \\ &= \sqrt{\left(\frac{\Delta T_{\text{v},\text{e}}}{\dot{Q}_{\text{in}}}\right)^2 + \left(\frac{\Delta T_{\text{v},\text{c}}}{\dot{Q}_{\text{in}}}\right)^2 + \left(\frac{(T_{\text{v},\text{e}} - T_{\text{v},\text{c}})}{\dot{Q}_{\text{in}}^2}\Delta \dot{Q}_{\text{in}}\right)^2} \end{aligned} \quad (10)$$

$$\begin{aligned} \Delta R_{\text{th},\text{out}} &= \sqrt{\left(\frac{\partial R_{\text{th},\text{out}}}{\partial T_{\text{v},\text{e}}}\Delta T_{\text{v},\text{e}}\right)^2 + \left(\frac{\partial R_{\text{th},\text{out}}}{\partial T_{\text{v},\text{c}}}\Delta T_{\text{v},\text{c}}\right)^2 + \left(\frac{\partial R_{\text{th},\text{out}}}{\partial \dot{Q}_{\text{out}}}\Delta \dot{Q}_{\text{out}}\right)^2} \\ &= \sqrt{\left(\frac{\Delta T_{\text{v},\text{e}}}{\dot{Q}_{\text{out}}}\right)^2 + \left(\frac{\Delta T_{\text{v},\text{c}}}{\dot{Q}_{\text{out}}}\right)^2 + \left(\frac{(T_{\text{v},\text{e}} - T_{\text{v},\text{c}})}{\dot{Q}_{\text{out}}^2}\Delta \dot{Q}_{\text{out}}\right)^2} \end{aligned} \quad (11)$$

### 1.3 Summary and Future Work

This report documents the status of the project as of the end of Summer 2001. A great deal of the experimental setup is complete and has been thoroughly calibrated. A new generation of  $\mu\text{CPLs}$  have been fabricated, and are in the process of being diced and instrumented. A major problem in the past has been making sure that the  $\mu\text{CPL}$  is hermetically sealed. To

address this problem, the vacuum-tightness of the  $\mu$ CPL will be evaluated using a helium leak detection unit. The  $\mu$ CPL will then be charged and tested in the vacuum chamber to determine the operating characteristics for various power input levels. Problems are anticipated with respect to the start-up behavior. The interaction between the  $\mu$ CPL and the working fluid reservoir is unknown at present, but will be controllable with an electrical heater tape mounted to the reservoir.



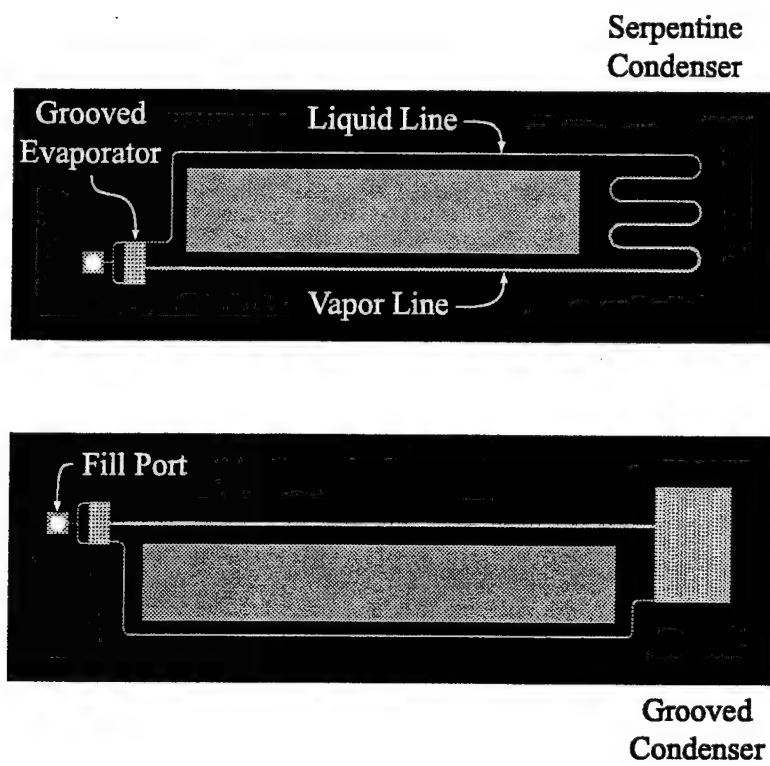


Figure 1: Variations of the basic  $\mu$ CPL design.

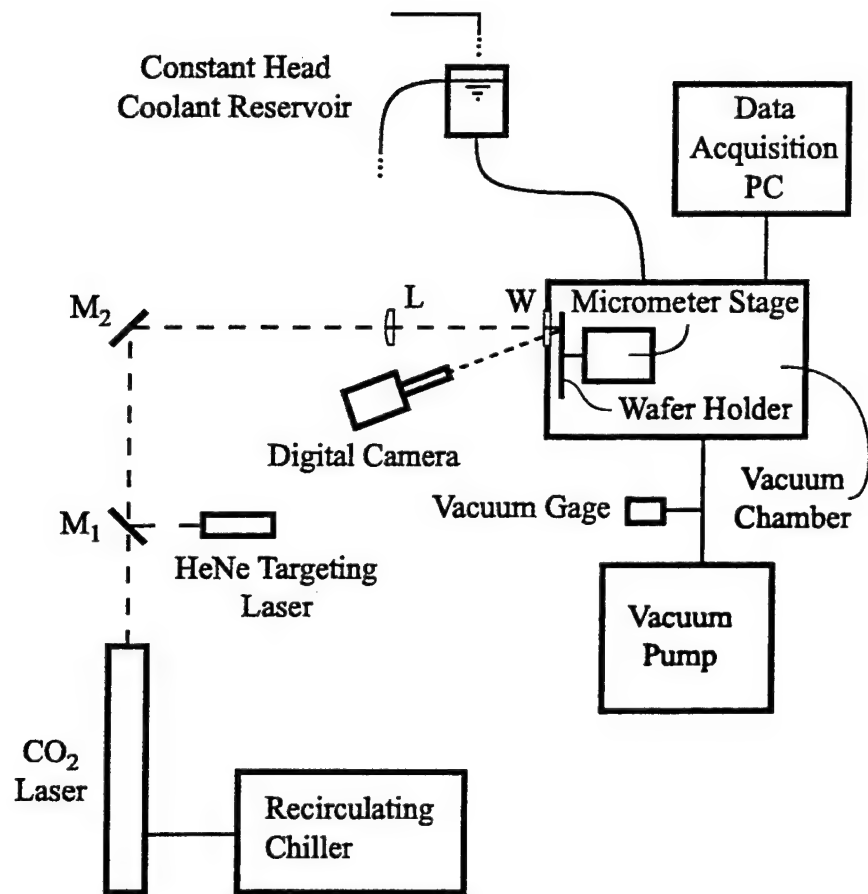


Figure 2: Schematic of  $\mu$ -CPL test setup.

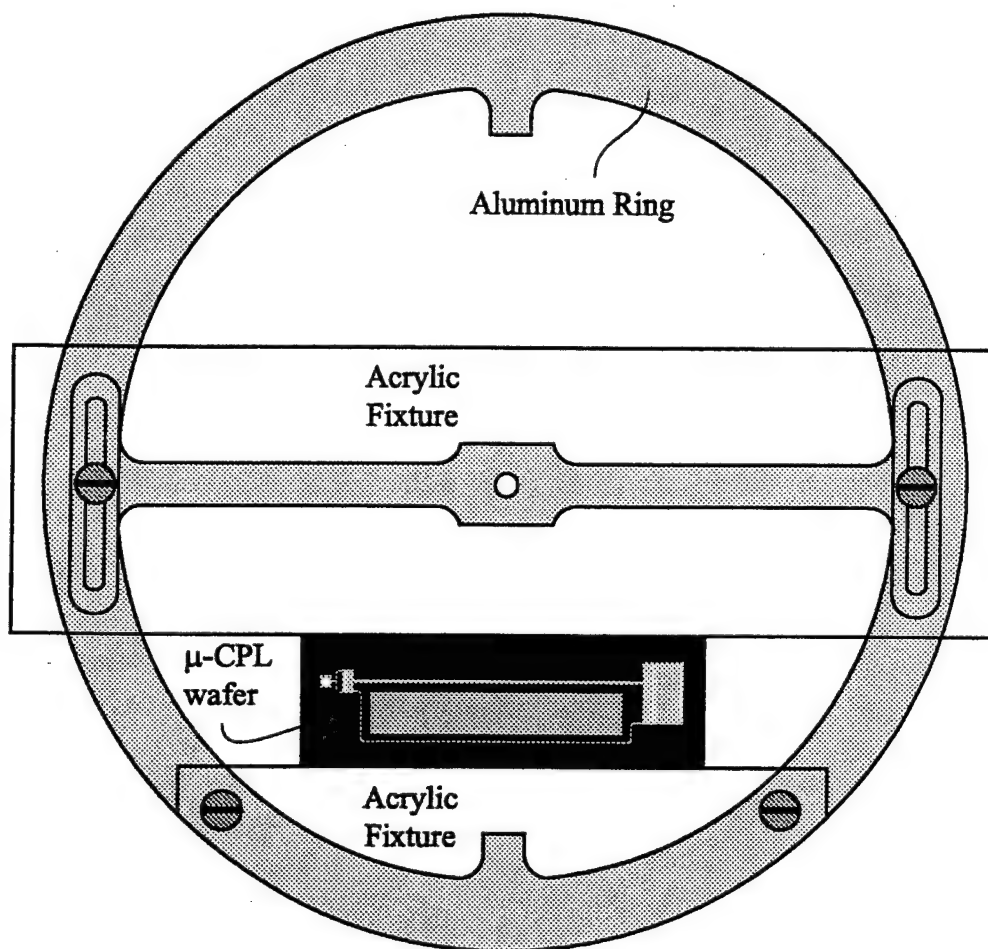


Figure 3: Mounting fixture for the  $\mu$ CPL.

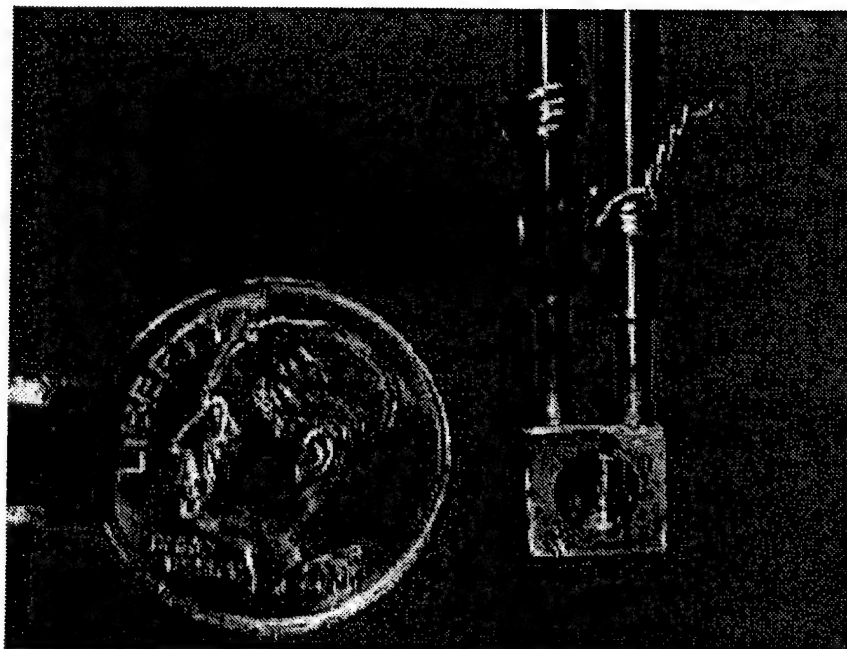


Figure 4: Photograph of the copper calorimeter.

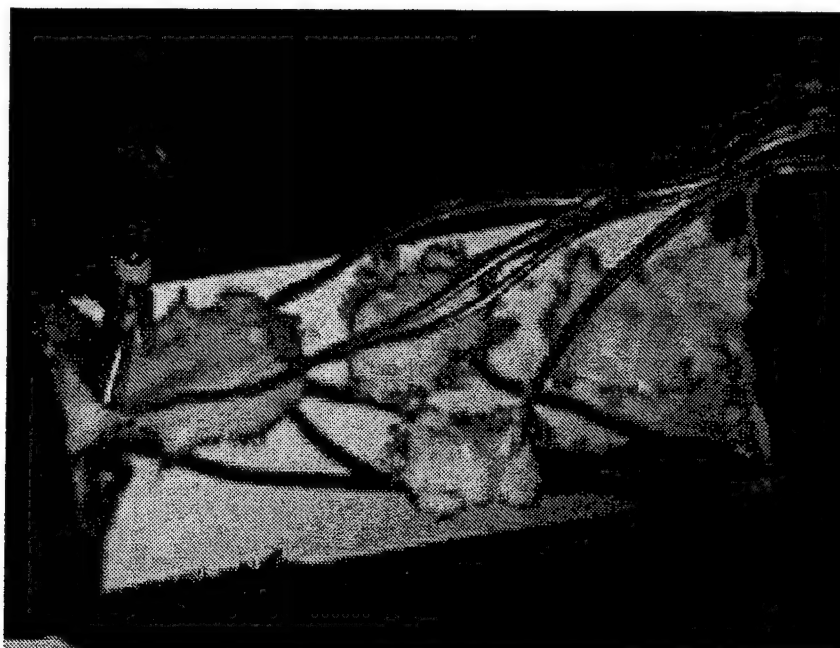


Figure 5: Photograph showing thermocouples adhered to the back of the  $\mu$ CPL wafer with vacuum epoxy. The stainless steel fill tube is on the left-hand side.

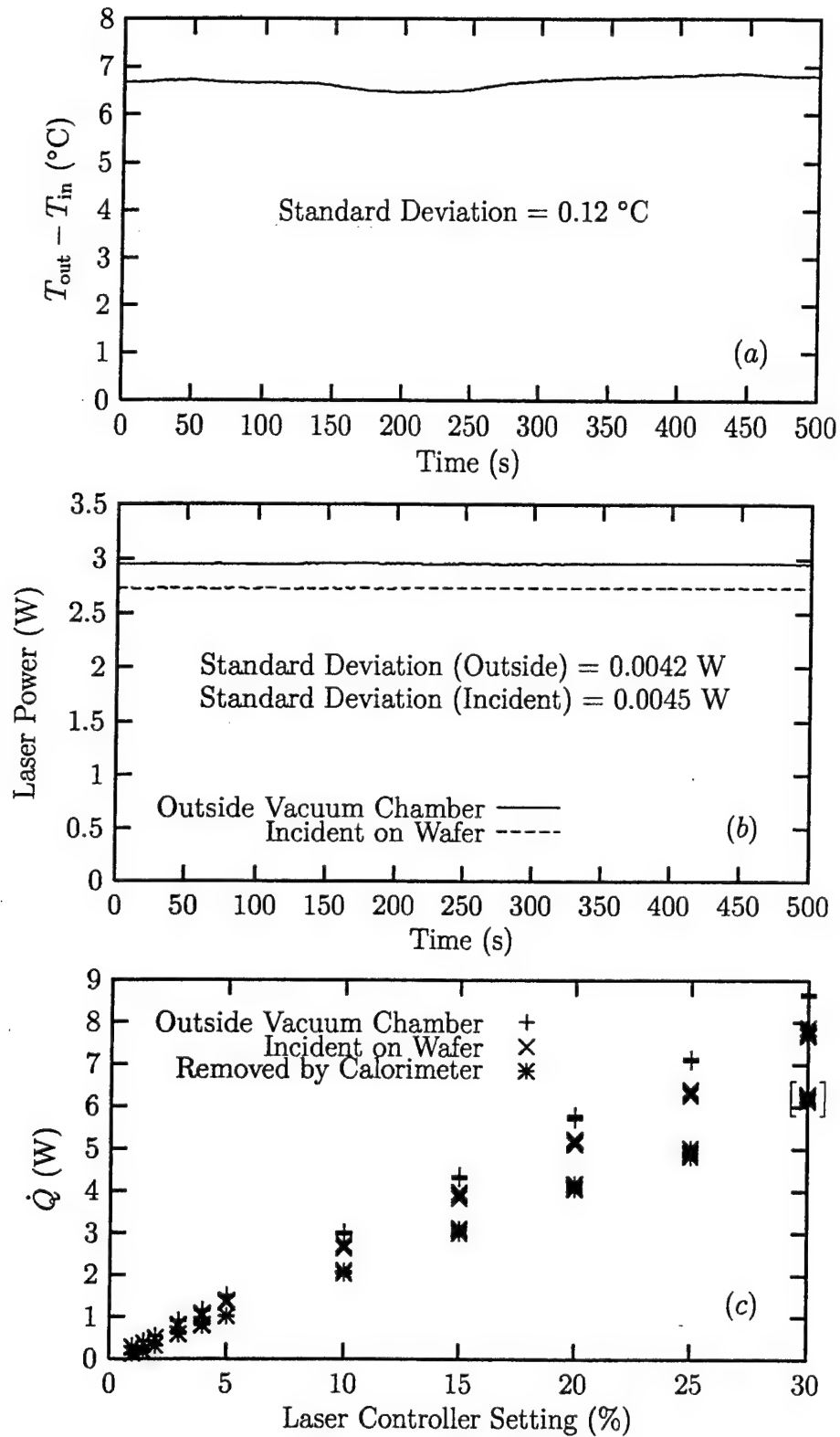


Figure 6: CO<sub>2</sub> laser calibration: (a) Typical calorimeter temperature increase trace (LCS = 10%); (b) Typical laser power measurement traces (LCS = 10%); (c) Heat rates versus LCS (Data points in square brackets were taken when the borosilicate glass melted on the wafer).

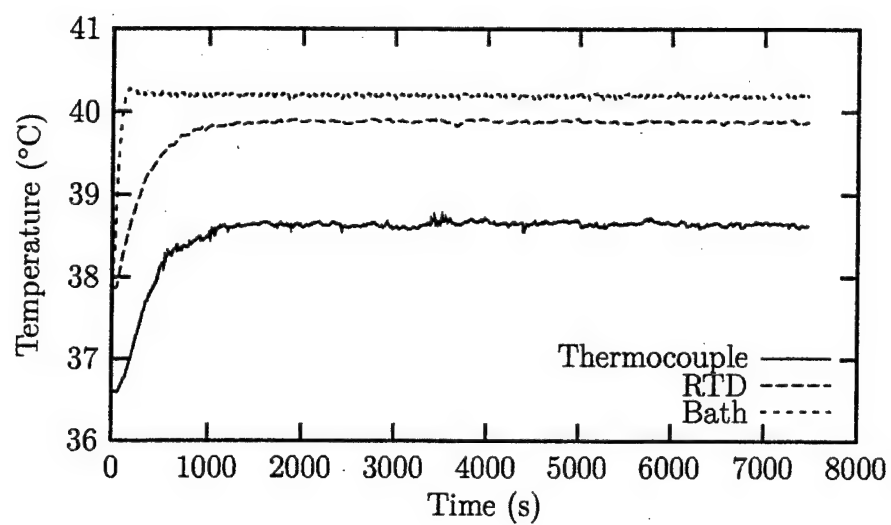


Figure 7: Temperature responses of a typical thermocouple, the resistance temperature detector, and the recirculating chiller bath.

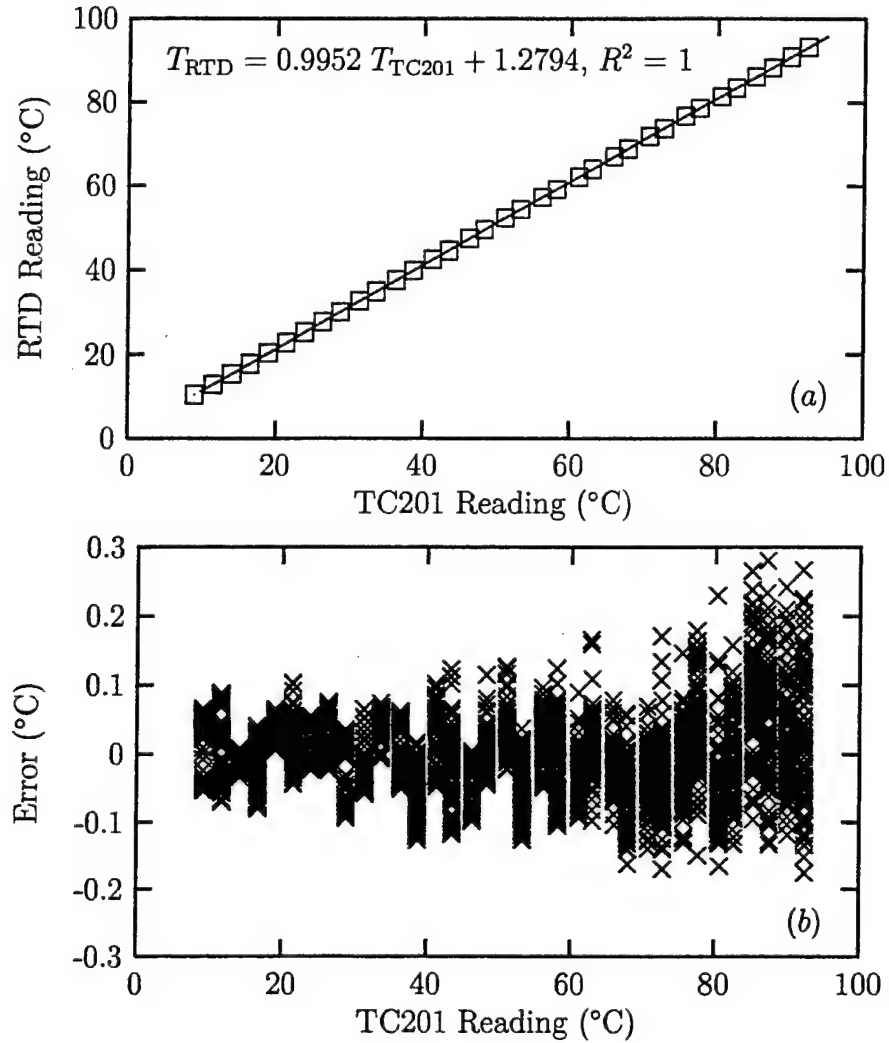


Figure 8: Temperature reading obtained during calibration (Thermocouple 201): (a) Temperature obtained by RTD vs. temperature reading from TC201; (b) Error obtained when substituting raw data into the linear best-fit equation for TC201.



Table 1: Laser calibration data.

LCS (%)	$\dot{Q}_{\text{window}} \pm \sigma$ (W)	$\dot{Q}_{\text{in}} \pm \sigma$ (W)	$\dot{Q}_{\text{out}} \pm \Delta \dot{Q}_{\text{out}}$ (W)
1	$0.295 \pm 0.0034$	$0.265 \pm 0.011$	$0.123 \pm 9\%$
1	$0.292 \pm 0.0025$	$0.261 \pm 0.0080$	$0.120 \pm 9\%$
1	$0.293 \pm 0.0044$	$0.253 \pm 0.0026$	$0.126 \pm 8\%$
1	$0.290 \pm 0.0063$	$0.256 \pm 0.0043$	$0.124 \pm 9\%$
1	$0.290 \pm 0.0010$	$0.273 \pm 0.0054$	$0.123 \pm 7\%$
1	$0.291 \pm 0.0042$	$0.271 \pm 0.0043$	$0.122 \pm 8\%$
1	$0.294 \pm 0.0023$	$0.268 \pm 0.0019$	$0.118 \pm 7\%$
1	$0.307 \pm 0.0028$	$0.287 \pm 0.0036$	$0.113 \pm 8\%$
1.5	$0.411 \pm 0.0077$	$0.360 \pm 0.012$	$0.186 \pm 8\%$
1.5	$0.408 \pm 0.0060$	$0.356 \pm 0.0058$	$0.183 \pm 6\%$
1.5	$0.409 \pm 0.0054$	$0.362 \pm 0.014$	$0.177 \pm 7\%$
1.5	$0.409 \pm 0.0053$	$0.358 \pm 0.0099$	$0.177 \pm 6\%$
1.5	$0.408 \pm 0.0012$	$0.380 \pm 0.0057$	$0.173 \pm 6\%$
1.5	$0.404 \pm 0.0079$	$0.380 \pm 0.0081$	$0.173 \pm 6\%$
1.5	$0.396 \pm 0.0019$	$0.376 \pm 0.0071$	$0.172 \pm 6\%$
1.5	$0.397 \pm 0.0023$	$0.370 \pm 0.0057$	$0.166 \pm 6\%$
2	$0.529 \pm 0.0011$	$0.489 \pm 0.0060$	$0.303 \pm 8\%$
2	$0.526 \pm 0.0037$	$0.490 \pm 0.0041$	$0.305 \pm 7\%$
2	$0.531 \pm 0.0047$	$0.489 \pm 0.0038$	$0.310 \pm 7\%$
2	$0.532 \pm 0.0045$	$0.489 \pm 0.0049$	$0.309 \pm 7\%$
2	$0.545 \pm 0.0052$	$0.502 \pm 0.0093$	$0.315 \pm 7\%$
2	$0.549 \pm 0.0016$	$0.495 \pm 0.0084$	$0.307 \pm 7\%$
2	$0.547 \pm 0.0025$	$0.484 \pm 0.0037$	$0.316 \pm 7\%$
2	$0.547 \pm 0.0035$	$0.479 \pm 0.0029$	$0.323 \pm 6\%$
3	$0.894 \pm 0.0089$	$0.777 \pm 0.0033$	$0.580 \pm 8\%$
3	$0.892 \pm 0.0055$	$0.795 \pm 0.015$	$0.593 \pm 8\%$
3	$0.890 \pm 0.0032$	$0.795 \pm 0.016$	$0.585 \pm 9\%$
3	$0.890 \pm 0.0014$	$0.810 \pm 0.012$	$0.589 \pm 7\%$
3	$0.915 \pm 0.0031$	$0.811 \pm 0.0049$	$0.586 \pm 9\%$
3	$0.921 \pm 0.0027$	$0.812 \pm 0.0059$	$0.588 \pm 7\%$
3	$0.922 \pm 0.0032$	$0.809 \pm 0.0032$	$0.585 \pm 8\%$
3	$0.921 \pm 0.0037$	$0.807 \pm 0.0031$	$0.594 \pm 8\%$
4	$1.15 \pm 0.0079$	$1.05 \pm 0.0054$	$0.811 \pm 8\%$
4	$1.14 \pm 0.0086$	$1.01 \pm 0.013$	$0.796 \pm 8\%$
4	$1.14 \pm 0.0082$	$1.01 \pm 0.0056$	$0.811 \pm 8\%$
4	$1.14 \pm 0.012$	$1.02 \pm 0.019$	$0.790 \pm 8\%$
4	$1.14 \pm 0.0018$	$1.06 \pm 0.0017$	$0.803 \pm 8\%$
4	$1.15 \pm 0.0061$	$1.06 \pm 0.0015$	$0.808 \pm 9\%$
4	$1.16 \pm 0.011$	$1.08 \pm 0.0040$	$0.789 \pm 8\%$
4	$1.17 \pm 0.0027$	$1.08 \pm 0.0064$	$0.820 \pm 9\%$

Table 2: Laser calibration data, continued.

LCS (%)	$Q_{\text{window}} \pm \sigma$ (W)	$Q_{\text{in}} \pm \sigma$ (W)	$Q_{\text{out}} \pm \Delta Q_{\text{out}}$ (W)
5	$1.49 \pm 0.015$	$1.33 \pm 0.016$	$1.01 \pm 6\%$
5	$1.48 \pm 0.0031$	$1.32 \pm 0.0024$	$1.01 \pm 6\%$
5	$1.48 \pm 0.0030$	$1.34 \pm 0.015$	$1.03 \pm 7\%$
5	$1.49 \pm 0.013$	$1.36 \pm 0.0058$	$1.02 \pm 5\%$
5	$1.50 \pm 0.0024$	$1.39 \pm 0.0018$	$1.01 \pm 5\%$
5	$1.49 \pm 0.0066$	$1.38 \pm 0.0059$	$1.03 \pm 5\%$
5	$1.49 \pm 0.0045$	$1.38 \pm 0.0064$	$1.02 \pm 5\%$
5	$1.49 \pm 0.0018$	$1.38 \pm 0.0034$	$1.02 \pm 5\%$
10	$2.96 \pm 0.010$	$2.66 \pm 0.036$	$2.08 \pm 4\%$
10	$2.97 \pm 0.016$	$2.64 \pm 0.024$	$2.07 \pm 3\%$
10	$2.97 \pm 0.012$	$2.72 \pm 0.039$	$2.09 \pm 4\%$
10	$2.97 \pm 0.0045$	$2.67 \pm 0.042$	$2.08 \pm 4\%$
10	$3.02 \pm 0.044$	$2.72 \pm 0.0042$	$2.06 \pm 3\%$
10	$2.97 \pm 0.0055$	$2.73 \pm 0.0035$	$2.10 \pm 4\%$
10	$2.96 \pm 0.0042$	$2.73 \pm 0.0045$	$2.04 \pm 4\%$
10	$2.96 \pm 0.0026$	$2.72 \pm 0.0040$	$2.03 \pm 6\%$
15	$4.31 \pm 0.024$	$3.90 \pm 0.057$	$3.07 \pm 5\%$
15	$4.30 \pm 0.014$	$3.91 \pm 0.0046$	$3.12 \pm 5\%$
15	$4.32 \pm 0.030$	$3.91 \pm 0.0040$	$3.10 \pm 6\%$
15	$4.31 \pm 0.028$	$3.83 \pm 0.083$	$3.06 \pm 5\%$
15	$4.37 \pm 0.032$	$3.92 \pm 0.069$	$3.00 \pm 8\%$
15	$4.35 \pm 0.016$	$3.98 \pm 0.0065$	$3.11 \pm 6\%$
15	$4.35 \pm 0.017$	$3.98 \pm 0.0047$	$3.12 \pm 4\%$
15	$4.35 \pm 0.012$	$3.98 \pm 0.0085$	$3.06 \pm 5\%$
20	$5.75 \pm 0.076$	$5.18 \pm 0.11$	$4.05 \pm 6\%$
20	$5.70 \pm 0.0051$	$5.22 \pm 0.14$	$4.05 \pm 7\%$
20	$5.75 \pm 0.093$	$5.10 \pm 0.0032$	$4.08 \pm 7\%$
20	$5.76 \pm 0.10$	$5.16 \pm 0.11$	$4.15 \pm 7\%$
20	$5.74 \pm 0.0038$	$5.22 \pm 0.0059$	$4.16 \pm 7\%$
20	$5.73 \pm 0.0046$	$5.22 \pm 0.0040$	$4.16 \pm 7\%$
20	$5.73 \pm 0.0057$	$5.22 \pm 0.0038$	$4.10 \pm 6\%$
20	$5.73 \pm 0.0049$	$5.22 \pm 0.0056$	$4.18 \pm 8\%$

Table 3: Laser calibration data, continued.

LCS (%)	$Q_{\text{window}} \pm \sigma$ (W)	$Q_{\text{in}} \pm \sigma$ (W)	$Q_{\text{out}} \pm \Delta Q_{\text{out}}$ (W)
25	$7.08 \pm 0.12$	$6.36 \pm 0.14$	$4.88 \pm 6\%$
25	$7.06 \pm 0.0063$	$6.26 \pm 0.039$	$4.81 \pm 7\%$
25	$7.07 \pm 0.0058$	$6.29 \pm 0.014$	$4.88 \pm 8\%$
25	$7.10 \pm 0.039$	$6.28 \pm 0.0068$	$4.91 \pm 5\%$
25	$7.10 \pm 0.040$	$6.32 \pm 0.052$	$4.99 \pm 6\%$
25	$7.09 \pm 0.020$	$6.30 \pm 0.035$	$4.85 \pm 7\%$
25	$7.11 \pm 0.039$	$6.40 \pm 0.0089$	$4.92 \pm 6\%$
25	$7.15 \pm 0.061$	$6.41 \pm 0.0052$	$5.02 \pm 6\%$
30	$8.65 \pm 0.028$	$7.68 \pm 0.0091$	$6.13 \pm 7\%$
30	$8.67 \pm 0.029$	$7.78 \pm 0.099$	$6.23 \pm 6\%$
30	$8.68 \pm 0.038$	$7.88 \pm 0.025$	$6.30 \pm 8\%$
30	$8.69 \pm 0.035$	$7.86 \pm 0.0078$	$6.16 \pm 8\%$
30	$8.62 \pm 0.052$	$7.67 \pm 0.023$	$6.30 \pm 5\%$
30	$8.63 \pm 0.036$	$7.67 \pm 0.028$	$6.21 \pm 6\%$
30	$8.61 \pm 0.0050$	$7.69 \pm 0.048$	$6.27 \pm 6\%$
30	$8.64 \pm 0.034$	$7.72 \pm 0.060$	$6.14 \pm 6\%$
1	$0.306 \pm 0.0015$	—	—
1	$0.312 \pm 0.0011$	—	—
1.5	$0.406 \pm 0.0057$	—	—
1.5	$0.429 \pm 0.0011$	—	—
2	$0.549 \pm 0.0012$	—	—
2	$0.546 \pm 0.0012$	—	—
3	$0.903 \pm 0.0030$	—	—
3	$0.909 \pm 0.0071$	—	—
4	$1.17 \pm 0.0032$	—	—
4	$1.17 \pm 0.0030$	—	—
5	$1.52 \pm 0.0021$	—	—
5	$1.50 \pm 0.0024$	—	—
10	$3.00 \pm 0.0074$	—	—
10	$3.02 \pm 0.0082$	—	—
15	$4.35 \pm 0.0048$	—	—
15	$4.34 \pm 0.0050$	—	—
20	$5.81 \pm 0.0066$	—	—
20	$5.77 \pm 0.010$	—	—
25	$7.14 \pm 0.044$	—	—
25	$7.14 \pm 0.039$	—	—

Table 4: Thermocouple calibration equations:  $T_{\text{actual}} = mT_{\text{reading}} + b$  (Valid ranges: TCs 201–210,  $10^{\circ}\text{C} \leq T_{\text{reading}} \leq 95^{\circ}\text{C}$ ; TCs 211 and 212,  $10^{\circ}\text{C} \leq T_{\text{reading}} \leq 40^{\circ}\text{C}$ ).

TC Number	$m$	$b$ ( $^{\circ}\text{C}$ )	Max Error ( $^{\circ}\text{C}$ )
201	0.9952	1.2794	0.30
202	0.9962	1.0023	0.30
203	0.9956	0.9031	0.30
204	0.9952	0.6704	0.30
205	0.9958	0.4097	0.30
206	0.9965	0.1150	0.25
207	0.9935	0.1410	0.40
208	0.9968	0.0079	0.15
209	0.9965	-0.0507	0.25
210	0.9964	0.0122	0.15
211	0.9936	0.1318	-0.093
212	0.9947	-0.0919	-0.054

#### 1.4 Nomenclature

$C_p$	specific heat, J/(kg-K)
LCS	laser controller setting, %
$m$	mass, kg
$\dot{m}$	mass flow rate, kg/s
$\dot{Q}$	rate of heat transfer, W
$\dot{Q}_{\text{in}}$	laser power incident on the blank wafer, W
$\dot{Q}_{\text{out}}$	power removed by the calorimeter mounted to the blank wafer, W
$\dot{Q}_{\text{window}}$	laser power incident on the window of the vacuum chamber, W
$R_{\text{th,in}}$	thermal resistance based on incident power, K/W
$R_{\text{th,out}}$	thermal resistance based on power removed by the calorimeter, K/W
$t$	time, s
$T_{\text{in}}$	calorimeter inlet temperature, K
$T_{\text{out}}$	calorimeter outlet temperature, K
$T_{\text{v,e}}$	vapor line temperature at the evaporator, K
$T_{\text{v,c}}$	vapor line temperature at the condenser, K

## **2 Design and Testing of a Thermodynamic Filling Station for Miniature Heat Pipes**

### **2.1 Abstract**

An experimental investigation was conducted to determine the feasibility of a thermodynamic process to fill miniature heat pipes. A heat pipe filling station has been designed and constructed, which consists of a vacuum pump, pressure gauges, thermocouples, a manifold of valves, a large evacuated volume, and an environmental test chamber. A general filling procedure has been formulated. The filling station has been tested and preliminary results have been obtained using a heat pipe. The target range for the working fluid fill amount for the present project is  $0.01$  to  $0.5 \text{ g} \pm 10\%$ . Preliminary results presented herein show that the current process is capable of filling miniature heat pipes with a mass of approximately  $0.7 \text{ g}$  with a repeatability of  $\pm 12\%$ . An analytical model that includes the effect of air within the fill station is presented. The analytical model overpredicts the experimental results by approximately  $26\%$ .

### **2.2 Introduction**

Suitably filling a heat pipe with a working fluid is a critical process in ensuring proper performance. The steps involved in any filling process include thoroughly cleaning the heat pipe, evacuating the heat pipe to remove all non-condensable gases, dispensing the proper amount of high purity working fluid, and finally, sealing the heat pipe. Variations from the optimal charge can adversely affect the performance of the heat pipe (Castle et al., 2000).

The performance of the heat pipe is very sensitive to the quantity of working fluid charged. A small variation in the fill amount can degrade the heat pipe performance, possibly preventing it from functioning. Undercharging can cause several effects, one of the more serious being premature dry-out at the evaporator section due to an unsaturated wick structure. This dry-out can cause an increase in local temperature, resulting in failure of the component being cooled due to inadequate heat removal (Gao et al., 2000). It is common to spend a considerable amount of time calculating the amount of charge required, then deliberately overcharging by  $10\text{-}20\%$  to prevent the possibility of undercharging (Peterson, 1994). Overcharging the heat pipe will also reduce performance by partially blocking the condenser

section due to the presence of a puddle of liquid.

There are several methods for filling heat pipes. However, few of these common practices are feasible for the 0.01 to 0.5 g fill quantities required for miniature heat pipes. One traditional method requires initially overfilling the heat pipe, heating it up to a desired operating temperature, venting off non-condensable gases, and then sealing the heat pipe once isothermal operation is attained. With miniature heat pipes, the fill quantities are too small and all the working fluid would probably be lost in this process.

Another method involves an evacuation and back-filling procedure (Castle et al., 2000). The heat pipe is attached to the heat pipe fill station, and both are then evacuated. The working fluid is then degassed using a freeze-thaw cycle or by boiling. Finally, the desired amount of working fluid is drawn into the heat pipe via a dispensing burette, and the heat pipe is sealed. The estimated uncertainties are well over 50% for this process applied to the small fill quantities of miniature heat pipes. The fill range for this process as tested by Castle et al. was 1.47 to 4.38 g  $\pm$  5%.

Gao et al. (2000) developed three different methods for filling miniature heat pipes. The first process proposed was a micro syringe method similar to the evacuation/back-filling procedure mentioned above. This method requires a micro syringe, a T-junction, and a vacuum pump. The syringe is filled with working fluid. The filling needle is then replaced with a new dry needle. The syringe and heat pipe are connected to the T-junction and the vacuum system. The heat pipe is then evacuated. Lastly, the syringe plunger is depressed, displacing all working fluid into the heat pipe. The main drawback of this process is that a certain amount of air inevitably enters the heat pipe.

The second and third methods are quite similar in theory and process. The thermodynamic equilibrium and capillary tubing method both include a vacuum system, working fluid source, and either a vacuum chamber (thermodynamic) or capillary tubing (capillary). The process starts by evacuating the system and all components. Next, the heat pipe is completely filled with working fluid and then attached to the filling station. A valve is opened and the heat pipe is exposed to the chamber/tubing, which results in the evaporation of some of the working fluid. A sudden drop in temperature occurs due to the evaporation process. The pressure then rises and an equilibrium point is achieved with the ambient. The

amount of liquid evaporated is determined by the chamber/tubing volume. In the capillary tubing method, the liquid removal is aided by pushing the extra liquid into the capillary tubing, but not by flashing. Fill ranges for the chamber process were given for two chambers sizes: Chamber 1 (1850 ml) 0.080 to 0.117 g (−16.8 to 21.0%); Chamber 2 (500 ml) 0.132 to 0.165 g (−11.1 to 11.2%).

The thermodynamic method mentioned by Gao et al. (2000) is very similar to the process chosen and implemented in the present research and experimentation. The objectives of the present experiment are to reduce the minimum fill amount beyond that given by Gao et al. by an order of magnitude (while maintaining an uncertainty of approximately 10%), and to compare the results of the present experiment with an analytical model of the thermodynamic process.

### 2.3 Analytical Model

The current heat pipe fill station is shown in Fig. 9(a), which can be divided into three volumes for analysis. The vacuum chamber volume extends to valves V1 and V2, and includes the tubing for the dial pressure gage, the thermocouple pressure gage, and the thermocouple probe. The manifold volume includes tubing from valves V2 and V3, the critical orifice, and the tubing and fittings up to the point at which the heat pipe is attached. The heat pipe volume includes the heat pipe envelope and the fill tube. During the filling process, the heat pipe is charged with liquid and attached to the fill station. The vacuum chamber is evacuated, but the manifold and heat pipe are at atmospheric pressure. Valve V2 is then opened, exposing the liquid in the heat pipe to the vacuum chamber. After a portion of the liquid evaporates, the system reaches a steady state condition. At this point, the heat pipe fill tube is sealed. The objective of this analysis is to determine the amount of liquid in the heat pipe at the final state by accounting for the presence of air within the system.

The mass of air initially within the vacuum chamber is given by the perfect gas relation.

$$m_{a,vc} = \frac{P_{vc,1}V_{vc}}{R_a T_1} \quad (12)$$

The initial pressure within the manifold is atmospheric since it is open to ambient conditions

when the heat pipe is attached to the fill station. The mass of air within the manifold is

$$m_{a,m} = \frac{P_{atm} V_m}{R_a T_1} \quad (13)$$

In general, the heat pipe volume at the initial state is taken up by the working fluid (liquid and vapor) at saturated conditions, which is in equilibrium with any air that may be present within the heat pipe. The mass of air within the heat pipe is dependent upon the method used for introducing the initial liquid charge. If the liquid is installed using a syringe, for instance, the amount of air is unknown. Therefore, the mass of air originally in the heat pipe will be varied from zero to the maximum value possible to determine the effect on the final conditions within the fill station. The maximum mass of air possible within the heat pipe can be determined by assuming that no vapor is present

$$m_{a,hp,max} = \frac{P_{atm} (V_{hp} - V_{l,1})}{R_a T_1} \quad (14)$$

where the volume of the liquid is based on the initial amount metered into the heat pipe.

$$V_{l,1} = m_{l,1} v_f \quad (15)$$

The total mass of air within the system is

$$m_{a,t} = m_{a,vc} + m_{a,m} + m_{a,hp} \quad (16)$$

After the heat pipe is connected to the fill station, valve V2 is opened and the evaporation process begins. It is assumed that the evaporation of the working fluid sweeps all of the air out of the heat pipe and into the manifold and vacuum chamber volumes. It is also assumed that the wick structure and the vertical orientation of the heat pipe prevent liquid droplets from being ejected from the heat pipe when it is mounted to the fill station. Finally, it is assumed that temperature for State 2 is equal to the initial temperature (prior to opening the valve V2). The final pressure in the system is the partial pressure of the working fluid at the ambient temperature. The final volume of air is

$$V_{a,2} = \frac{m_{a,t} R_a T_1}{P_{v,2}} \quad (17)$$

The volume occupied by the working fluid is

$$V_{wf,2} = V_t - V_{a,2} \quad (18)$$



Using the definition of quality, the mass of working fluid in the vapor state is

$$m_{v,2} = \frac{V_{wf,2} - m_{l,1}v_f}{v_{fg}} \quad (19)$$

The mass of working fluid in the liquid state is determined using the continuity equation.

$$m_{l,2} = m_{l,1} - m_{v,2} = m_{l,1} - \left( \frac{V_{wf,2} - m_{l,1}v_f}{v_{fg}} \right) \quad (20)$$

## 2.4 Experimental Setup

The current filling station is shown schematically in Fig. 9(a) and Fig. 10. The station consists of an aluminum vacuum chamber, a stainless steel manifold of valves and interconnecting tubing, a critical orifice plate and a mechanical vacuum pump. Initially, the open heat pipe container is charged with liquid working fluid, which is measured using a precision scale (Ohaus Explorer Model E01140). The heat pipe is then attached to the filling station as shown in Fig. 9(a). The vacuum chamber is evacuated and subsequently isolated from the vacuum pump. Valve V2 is then opened to expose the working fluid in the heat pipe to the reduced pressure within the vacuum chamber. This initiates evaporation of the liquid working fluid, which halts when the system reaches a steady state condition with the ambient. The ambient temperature is controlled by placing the entire filling station into an environmental chamber (Thermotron,  $\Delta T_\infty \simeq 1.0^\circ\text{C}$ ). Temperatures within the vacuum chamber and on the surface of the heat pipe were measured using Type T thermocouples and a data acquisition system (Fluke 2286A Data Logging System). The pressure within the vacuum chamber was tracked using a thermocouple vacuum gauge and reader (Varian Model 0531 and Model 804-A) and a dial absolute pressure gauge (Wallace and Tiernan). A mechanical vacuum pump (Duo Seal Model 1397) was employed to evacuate the system.

As the preliminary testing of the system progressed, it was found that a device was needed to control the flow of working fluid from the heat pipe to the vacuum chamber. When the valve V2 is initially opened, a portion of the liquid could flash off into the vacuum chamber, which could result in a slug of liquid being ejected from the heat pipe container. A critical orifice design was implemented to slow the evaporation process by restricting the maximum mass flow rate of the vapor from the heat pipe. The cross-sectional area of the hole in the orifice plate was calculated using the following expression, which is based on the assumption

that the flow is choked at the throat.

$$A^* = \dot{m} \left[ P_0 \sqrt{\frac{k}{R_w T_0}} \left( \frac{2}{k+1} \right)^{\left( \frac{k+1}{2(k-1)} \right)} \right]^{-1} \quad (21)$$

Once the area was known, the orifice plate was constructed using copper plate and placed in between two flanges (Fig. 11(a)). Three orifice plates were made with three different orifice diameters for experimentation:  $D_o = 0.203$  mm (0.008 in.), 0.381 mm (0.015 in.) and 0.762 mm (0.0300 in.). A photograph of the orifice plate installed in the filling station is shown in Fig. 11(b).

It was necessary to accurately determine all of the volumes of the fill station, which included all of the components, the chamber, and the heat pipe, for the calculations made in the mathematical model. All volumes were found either by calculations or by given values in the manufacturer manuals. Since all of the volumes were cylindrical, the uncertainty of the volume  $\Delta V$  was found by using the root-sum-square method

$$\Delta V = \sqrt{\left( \frac{\partial V}{\partial r} \Delta r \right)^2 + \left( \frac{\partial V}{\partial h} \Delta h \right)^2} \quad (22)$$

$$= \sqrt{(2\pi r h \Delta r)^2 + (\pi r^2 \Delta h)^2} \quad (23)$$

where the uncertainties of the measured values,  $\Delta r$  and  $\Delta h$ , were comprised of the readability or the uncertainty of the measurement tool. The dial caliper used had a readability of 0.0254 mm (0.001 in.), and a readability per measurement of 0.0254 mm (0.001 in.). The scale used had a readability of 0.396 mm (1/64 in.) and a readability of 0.793 mm (2/64 in) per measurement. The measured values for all of the components and the total volumes are given in Table 5.

## 2.5 Results and Discussion

Results of preliminary tests are shown in Fig. 12, where the experimental data are compared to the analytical model. While the model significantly over-predicts the experimental data (approximately 26%), the model matches the slope of the linear best-fit curve for the experimental data fairly well. The curve labelled "Analytical, No Air" shows the results when no air is present in the system; i.e., the vacuum chamber, manifold and heat pipe are

completely evacuated. Under this condition, the amount of liquid left in the heat pipe is less than with air present, as expected. It was determined that assuming the heat pipe did not contain any air at the start of the process had a negligible effect on the results. The data points presented fit the linear curve to within  $\pm 12\%$ , but more data points are needed to fully evaluate the repeatability of the system.

## 2.6 Conclusions and Future Directions

Initial testing of the heat pipe filling station has verified the viability of the thermodynamic process. Inconsistencies between the analytical model and the experimental data will require further investigations into methods of improving the agreement. In order to reduce the amount of air within the system, a combined filling station is proposed as shown in Fig. 9(b), where a conventional back-filling station is attached to the current thermodynamic filling station. The merits and drawbacks of this combined station still need to be evaluated.

## 2.7 References

Castle, R., Thomas, S., and Yerkes, K., 2000, "The Effect of Working Fluid Inventory on the Performance of Revolving Helically-Grooved Heat Pipes," *ASME Journal of Heat Transfer*, Vol. 123, pp. 120-129.

Cengel, Y., and Boles, M., 2002, *Thermodynamics: An Engineering Approach*, 4th Edn., McGraw-Hill, Boston.

Gao, M., and Cao, Y., Jones, K., and Zampino, M., 2000, "Ceramic Miniature Heat Pipes and Liquid Charging Methods," *Proceedings of the ASME National Heat Transfer Division-2000* Vol. 4. pgs. 429-434.

Miller, R., 1989, *Flow Measurement Engineering Handbook*, 2nd Edn., McGraw-Hill, New York.

Peterson, G., 1994, *An Introduction to Heat Pipes: Modeling, Testing and Applications*, Wiley.

## 2.8 Nomenclature

$A^*$	cross-sectional area of the critical orifice throat, $m^2$
$h$	cylinder height, m

$k$	ratio of specific heats
$m_{a, hp}$	mass of air in the heat pipe, kg
$m_{a, hp, max}$	maximum possible mass of air in the heat pipe, kg
$m_{a, m}$	mass of air in the manifold, kg
$m_{a, t}$	total mass of air in the filling station, kg
$m_{a, vc}$	mass of air in the vacuum chamber, kg
$m_{l, 1}$	initial mass of liquid working fluid in the heat pipe, kg
$m_{l, 2}$	mass of saturated working fluid liquid in the heat pipe at State 2, kg
$m_{v, 2}$	mass of saturated working fluid vapor in the filling station at State 2, kg
$\dot{m}$	mass flow rate, kg/s
$P_{atm}$	atmospheric pressure, Pa
$P_{v, 2}$	partial pressure of the saturated working fluid vapor at State 2, Pa
$P_{vc, 1}$	air pressure in the vacuum chamber at State 1, Pa
$P_0$	stagnation pressure, Pa
$r$	cylinder radius, m
$R_a$	particular gas constant of air, J/(kg-K)
$T_0$	stagnation temperature, K
$T_1$	initial system temperature, K
$v_f$	specific volume of saturated liquid, m <sup>3</sup> /kg
$v_{fg}$	$v_g - v_f$ , m <sup>3</sup> /kg
$v_g$	specific volume of saturated vapor, m <sup>3</sup> /kg
$V$	volume, m <sup>3</sup>
$V_{a, 2}$	volume of air at State 2, m <sup>3</sup>
$V_{hp}$	heat pipe volume, m <sup>3</sup>
$V_{l, 1}$	initial volume of liquid working fluid in the heat pipe, m <sup>3</sup>
$V_m$	manifold volume, m <sup>3</sup>
$V_t$	total volume of the filling station and heat pipe, m <sup>3</sup>
$V_{vc}$	vacuum chamber volume, m <sup>3</sup>
$V_{wf, 2}$	volume occupied by the working fluid at State 2, m <sup>3</sup>
$\Delta h$	uncertainty in measured height, m

$\Delta r$       uncertainty in measured radius, m  
 $\Delta V$       uncertainty in measured volume, m

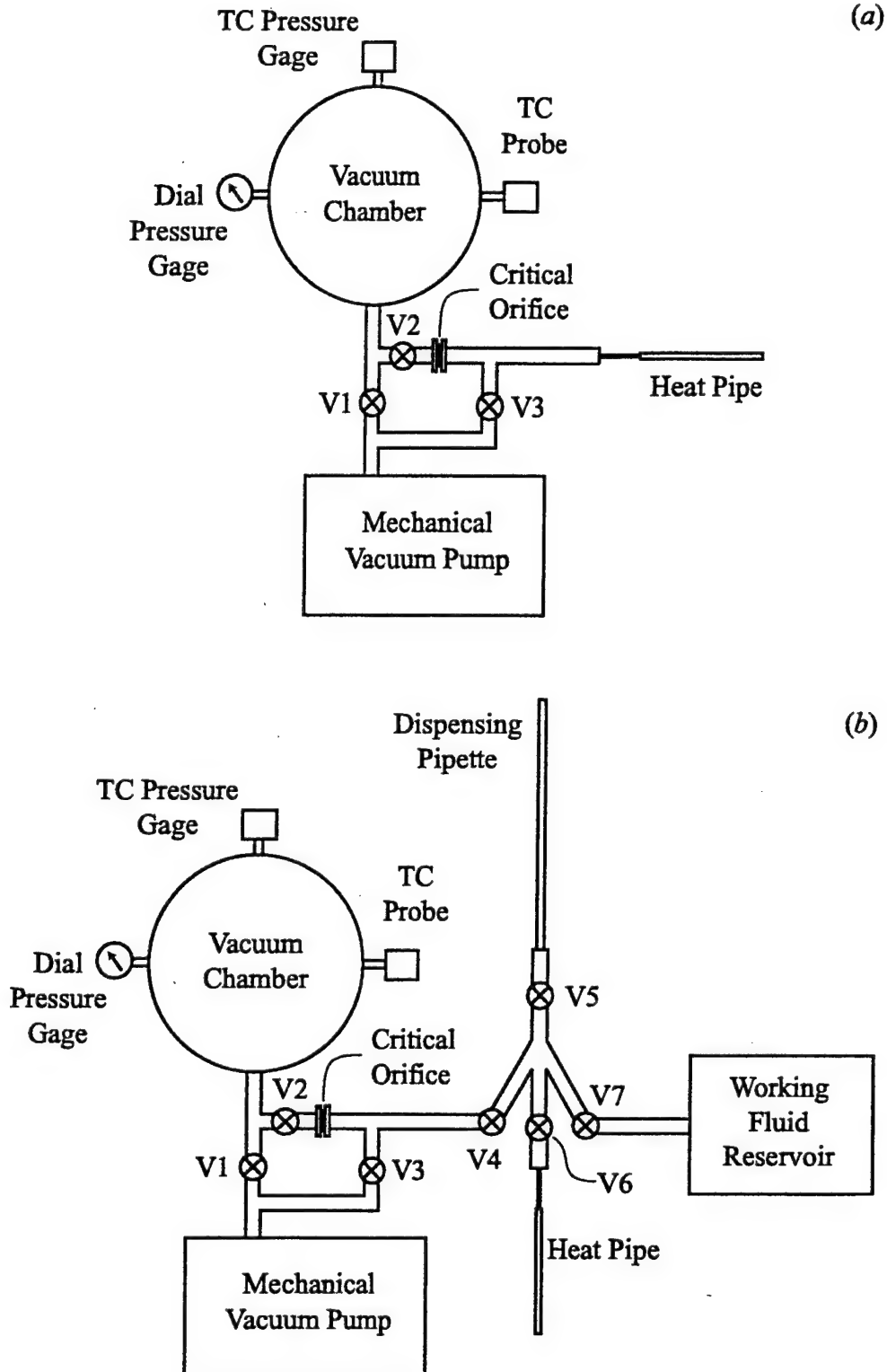


Figure 9: Schematic of the heat pipe filling station: (a) Current system; (b) System incorporating a standard filling station.

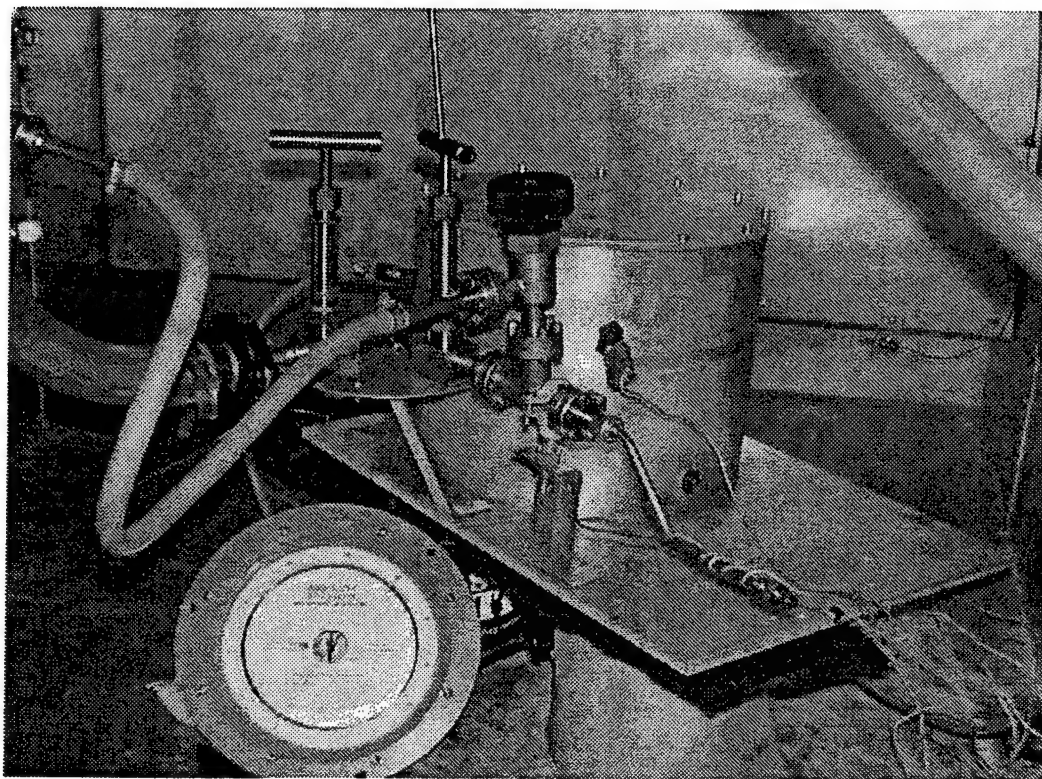


Figure 10: Thermodynamic heat pipe filling station.

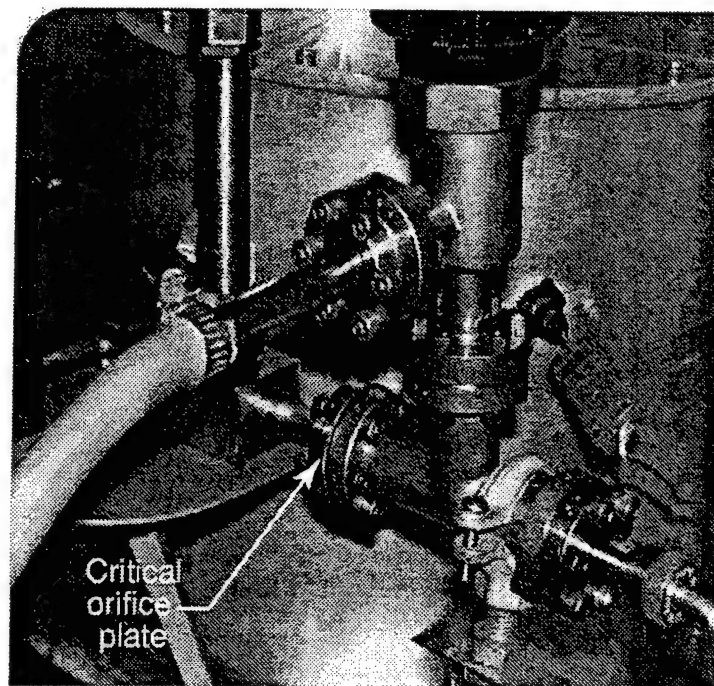
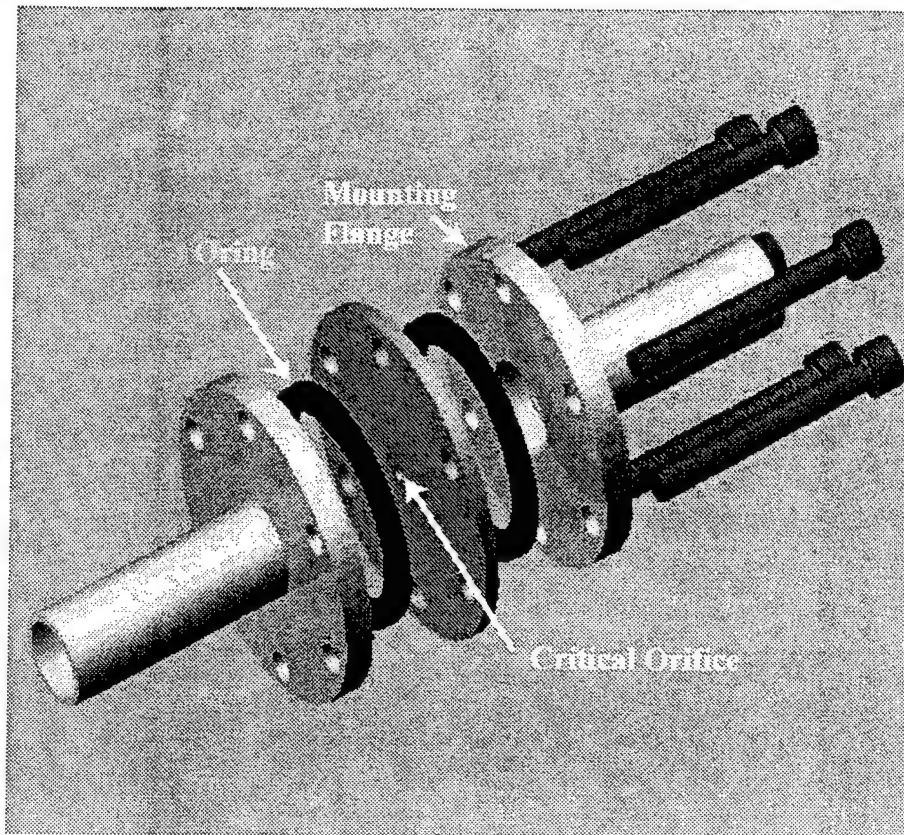


Figure 11: Critical orifice plate: (a) Internal design; (b) Installation in the filling station.



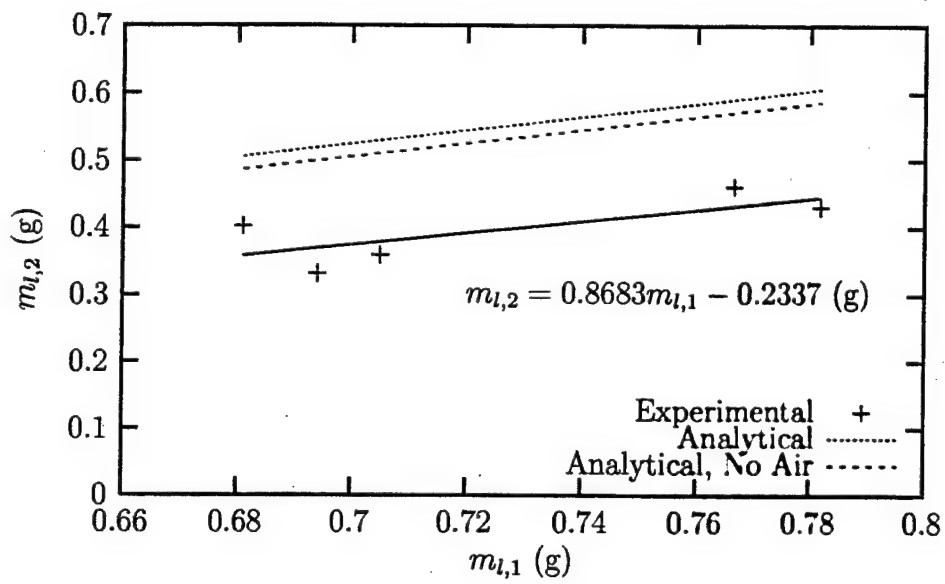


Figure 12: Mass of liquid in the heat pipe at State 2 versus initial liquid charge ( $m_{a,hp} = 0$ ,  $P_{vc,1} = 30$  mTorr,  $T_1 = 25^\circ\text{C}$ ,  $P_{atm} = 10^5$  Pa).

### **3 Acceleration Testing of Three Raytheon Heat Pipes using the AFRL/PRPS Centrifuge Table**

#### **3.1 Abstract**

The purpose of this experiment was to determine the effect of adverse longitudinal acceleration on the operation of three heat pipes provided by Raytheon. The heat pipe assembly (as delivered) was mounted to a centrifuge table such that the evaporator sections were closer to the center of the table than the condenser sections, which resulted in an adverse acceleration condition. The start-up test is described as follows: Rotate the centrifuge table for five min. at the prescribed acceleration level (5-g or 10-g), stop the rotation, wait for 5 s, then apply a fixed power input to the evaporator. The burst test consists of the following: Apply a fixed power input to the evaporator, allow the heat pipe to reach steady-state operation, rotate the centrifuge table at the prescribed acceleration level (5-g or 10-g) for 5 s, then stop the rotation. During the start-up tests, it was found that the 3-inch and 6-inch heat pipes (3IHP and 6IHP) were not affected, but the 9-inch heat pipe (9IHP) showed signs of a deprime condition. The burst tests resulted in the 3IHP and 9IHP becoming deprimed to a significant degree. The response time of the 9IHP to the initial start-up was significantly longer than the other heat pipes.

#### **3.2 Experimental Setup**

The heat pipe experiments were carried out on an eight-foot diameter horizontal centrifuge table at Wright-Patterson Air Force Base (AFRL/PRPS). This table was driven by a 20-hp DC motor (General Electric) and was controlled remotely for safety. A data acquisition unit (Keithley Model 500A) with a personal computer running data logging software (Viewdac) was used to collect temperature and acceleration profiles. The heat pipe assembly was attached to the centrifuge table as shown in Figs. 13 and 14. An accelerometer (Columbia Research Laboratories Model SA-307IIPTX) was used to measure the acceleration at the lengthwise center of the heat pipes. Temperature signals were conditioned and amplified on the centrifuge table. These signals were transferred off the table through the instrumentation slip ring assembly, which was completely separate from the power slip ring assembly to reduce electronic noise. Conditioning the temperature signals on the centrifuge

Name	$r$ (in)	$h$ (in)	$V$ (in <sup>3</sup> )	$\Delta V$ (in <sup>3</sup> )	Percent Error
Large Cylinder	4.516	8.031	514.6	7.4	1.4
Cylinder Weld	4.516	0.312	-1.385	0.013	0.94
Hole	0.233	0.300	0.051	0.0005	0.98
Hole	0.213	0.150	0.021	0.0002	0.95
Hole	0.200	0.285	0.036	0.0004	1.1
Hole	0.218	0.160	0.024	0.0003	1.2
Hole	0.225	0.145	0.023	0.0003	1.3
Hole	0.183	0.170	0.018	0.0002	1.1
Hole	0.168	0.340	0.030	0.0004	1.3
Stainless Tubing	0.125	1.375	0.068	0.0019	2.8
Stainless Tubing	0.125	3.25	0.160	0.003	1.9
Dial Gauge Tubing	0.063	21.0	0.258	0.0083	3.2
Male Extension	0.093	1.325	0.036	0.0011	3.1
TC Vacuum Gauge	0.132	2.00	0.110	0.0024	2.2
TC Probe Fitting	0.125	0.250	0.012	0.0015	12
Reducing Bushing	0.140	0.188	0.012	0.0019	16
Swagelok	0.125	0.50	0.025	0.0016	6.4
Swagelok to Pipe	0.125	1.00	0.049	0.0017	3.5
Bellows Valve	N/A	N/A	0.153	0.0015	0.98
Stainless Tubing	0.125	1.50	0.074	0.0019	2.6
O-ring Fitting	0.093	0.375	0.010	0.0009	9.0
Mini T Jcn	0.313	3.00	0.920	0.0113	1.2
Mini T Jcn	0.313	1.125	0.345	0.0098	2.8
Varian Valve	0.188	1.50	0.166	0.0039	2.3
Bellows Valve	N/A	N/A	0.076	0.0015	2.0
Heat Pipe	N/A	N/A	0.047	0.001	2.1

Table 5: Heat pipe filling station volume data ( $V_{vc} = 514.3 \text{ in}^3 = 8.428 \times 10^{-3} \text{ m}^3$ ,  $V_m = 1.591 \text{ in}^3 = 2.607 \times 10^{-5} \text{ m}^3$ ,  $V_{hp} = 0.047 \text{ in}^3 = 7.702 \times 10^{-7} \text{ m}^3$ ,  $V_t = 8.455 \times 10^{-3} \text{ m}^3$ ).

table eliminated difficulties associated with creating additional junctions within the slip ring assembly.

Power was supplied to the heat pipe evaporator section by a precision power supply (Kepco Model ATE 150-7M) through power slip rings to the table. The input power was calculated using the current and voltage readings. While the current reading could be made directly using a precision ammeter, the voltage across the electric heater had to be measured on the rotating table because voltage drops were noted between the control room and the table, regardless of the size of wire used. Therefore, the voltage at the heater was obtained through the instrumentation slip ring assembly and measured by a precision voltmeter (Hewlett Packard Model 3478A).

### **3.3 Experimental Procedure**

Two separate procedures were developed to examine the performance of the heat pipes under adverse acceleration conditions. The start-up test and the burst test are discussed in this section. In all of the experiments, the table was allowed to rotate slowly to prevent damage to the instrumentation and power slip rings. This baseline rotational speed was  $\omega = 0.0329$  rad/s, which imposed a radial acceleration of  $a_r = 1.24 \times 10^{-4}$ -g. While a baseplate heater was present on the heat pipe assembly, it was not used during these tests. In addition to recording the temperatures and accelerations to computer data files continuously during the test, the temperature, acceleration, and heater power information (voltage and current) were recorded into a logbook at intervals during the testing. For all tests, the electrical power input to the evaporator heater was approximately 17 W. To prevent damage to the heater mounted to the heat pipe evaporator section, a maximum evaporator temperature of 115°C was imposed. Each test was run three times to evaluate the repeatability of the experimental procedure.

#### **Burst test procedure**

1. Turn on the data logging software to record baseline readings.
2. Turn on the power to the heater.
3. Allow the heat pipe to reach steady-state operation.

4. After about 25 min. of steady-state operation, bring the table rapidly to the desired radial acceleration by increasing the rotational speed.
5. Hold this acceleration for 5 s.
6. Rapidly decelerate the table back to the baseline rotational speed.
7. Monitor the temperatures in case of evaporator dry-out.
8. If the pipe returns to steady-state operation, record data for about 20 min.
9. Repeat steps 4 through 7, using the same acceleration.
10. If the heat pipe returns to steady-state operation after the second burst, record data for about 20 min.
11. Shut off the heater power.
12. Record the cool down process for several minutes.
13. Turn off the data acquisition software and download the data files.

#### **Start-up test procedure**

1. Start the data logging software to record baseline data.
2. Increase the rotational speed of the table to reach the desired radial acceleration. Allow the table to rotate at this speed for 5 min.
3. Bring the table rapidly back down to its baseline speed.
4. Wait 5 s and then turn on the evaporator heater.
5. Allow the heat pipe to reach steady-state operation.
6. Run the heat pipe at steady-state condition for about 30 min.
7. Turn off the power to the heater.
8. Record the cool down process for several minutes.

9. Stop the data logging software and download the data files.

For each test, plots were generated of temperature vs. time and radial acceleration vs. time.

### 3.4 Results and Discussion

Three heat pipes have been tested to determine their thermal performance characteristics when subjected to adverse acceleration conditions. The heat pipe assembly was mounted to a centrifuge table at AFRL/PRPS to impose a radial acceleration along the axial direction of the heat pipes. Included in this section are typical temperature-time traces, steady-state measurements of the temperature difference between the evaporator and middle (adiabatic) thermocouples, and initial start-up times, both for stationary start-ups and start-ups following long periods of acceleration.

Figure 15 presents typical temperature-time traces during a 5-g start-up test. All three heat pipes reached the steady state in a relatively short time. This steady-state condition was maintained for approximately 30 min., and then the heater power was turned off. For the 3IHP and 6IHP, the temperature difference between the evaporator and adiabatic sections ( $\Delta T_{ea}$ ) was lower than that for the 9IHP. This temperature difference was chosen as an indicator of wick priming based on previous experience with heat pipes ([1]–[8]). The evaporator-adiabatic temperature differences for all of the start-up tests are shown in Fig. 16, where  $\Delta T_{ea}$  was significantly higher and more scattered for the 9IHP. Both of these points indicate that the wick was poorly primed prior to start-up for the 9IHP.

Figure 17 shows the results for four burst tests. In Fig. 17(a), the 3IHP was allowed to reach a steady-state condition while the centrifuge table was rotating at its baseline speed. At approximately  $t = 2500$  s, the rotational speed was increased such that  $a_r = 5.0$ -g for 5 s, and then the speed was reduced to the baseline. While the adiabatic and condenser temperatures remained fairly constant, the evaporator temperature increased significantly, indicating a partial dry-out event. The heat pipe was again allowed to reach another steady-state condition, and another burst test was carried out at approximately  $t = 4500$  s. The evaporator temperature increased further, and the power to the heater was shut off due to a run-away dry-out situation.

Figures 17(b) and 17(c) compare two burst tests for the 6IHP. Of particular interest is the initial start-up period shown in Fig. 17(b), where a wick priming event occurred at approximately  $t = 600$  s. In this event, the temperature difference between the evaporator and adiabatic sections was initially high ( $\Delta T_{ea} \simeq 23^\circ\text{C}$ ). After the wick primed, the adiabatic temperature increased dramatically, which decreased the temperature difference to  $\Delta T_{ea} \simeq 11^\circ\text{C}$ . Two burst tests were carried out in Fig. 17(b) at  $t = 2500$  and  $4000$  s, and the 6IHP did not deprime in either case. In Fig. 17(c), the wick did not prime during start-up, and the temperature difference remained at  $\Delta T_{ea} \simeq 22^\circ\text{C}$  prior to the acceleration burst. Again, two burst tests were performed ( $t = 2500$  and  $4500$  s). In each of these tests, the temperature difference actually decreased slightly, showing that the heat pipe wick structure was partially primed by the acceleration burst.

Figure 17(d) shows the performance of the 9IHP during a burst test with bursts at  $t = 2500$  and  $4000$  s. Initially, the heat pipe was primed with a very low temperature difference ( $\Delta T_{ea} \simeq 7^\circ\text{C}$ ). After the first burst test, the adiabatic temperature decreased significantly which resulted in  $\Delta T_{ea} \simeq 25^\circ\text{C}$ . The second burst test resulted in a run-away dry-out situation, so the test was halted.

Figure 18 shows the steady-state data for all of the burst tests, except for the run-away dry-out situations, since steady-state data could not be collected. This test had a detrimental impact on the wick priming for the 3IHP and the 9IHP, where  $\Delta T_{ea}$  increased after the burst test. The 6IHP was less sensitive to the burst-test conditions in comparison to the other heat pipes.

The response times of the heat pipes to the initial application of the heat load are displayed in Fig. 19. These times were calculated using the 63% time-constant method, where the time constant is defined as the time required for the evaporator temperature to reach 63% of its steady-state value. These data include the initial start-up responses for both the start-up tests and the burst tests, where the power to the evaporator is first energized. The responses due to the actual burst tests (immediately after the radial acceleration was increased and then decreased) were not included due to difficulties in defining an appropriate time constant. The time constants for all three heat pipes were very repeatable, with the time constant for the 9IHP being more than twice as long as those of the other heat pipes.

It is believed that the 3IHP was not properly charged based on the following observations.

1. During the start-up tests,  $\Delta T_{ea}$  was higher for the 3IHP than the 6IHP (Fig. 16).
2. For the burst tests,  $\Delta T_{ea}$  for the 3IHP was greater than both the 6IHP and the 9IHP (Fig. 18).
3. The response time for the 3IHP (52 s) was higher than the 6IHP (44 s) (Fig. 19).

It was expected that the 3IHP would perform with a lower  $\Delta T_{ea}$  and with a shorter response time than the 6IHP due to the shorter effective heat pipe length of the 3IHP.

### 3.5 Conclusions

Based on the experiments described above, the following conclusions have been made concerning the performance of the three heat pipes under adverse longitudinal acceleration conditions:

1. During the start-up tests, the 9IHP showed signs of a deprimed wick structure.
2. The burst tests caused the 3IHP and the 9IHP to become deprimed.
3. The start-up response time for the 9IHP was significantly higher than the other heat pipes (more than double).
4. The 3IHP may not have been properly charged with working fluid.

### References

- [1] Castle, M., Thomas, S., and Yerkes, K., 2001, "The Effect of Working Fluid Inventory on the Performance of Revolving Helically-Grooved Heat Pipes," *ASME Journal of Heat Transfer*, Vol. 123, pp. 120-129.
- [2] Klasing, K., Thomas, S., and Yerkes, K., 1999, "Prediction of the Operating Limits of Revolving Helically-Grooved Heat Pipes," *ASME Journal of Heat Transfer*, Vol. 121, pp. 213-217.



- [3] Thomas, S., Klasing, K., and Yerkes, K., 1998, "The Effects of Transverse Acceleration-Induced Body Forces on the Capillary Limit of Helically-Grooved Heat Pipes," *ASME Journal of Heat Transfer*, Vol. 120, pp. 441-451.
- [4] Thomas, S., and Yerkes, K., 1997, "Quasi-Steady State Performance of a Heat Pipe Subjected to Transient Acceleration Loadings," *AIAA Journal of Thermophysics and Heat Transfer*, Vol. 11, pp. 306-309.
- [5] Klasing, K., Thomas, S., and Yerkes, K., 1997, "CAPLIM: A VISUAL BASIC Program to Calculate the Capillary Limit of an Axially-Grooved Heat Pipe," *Proceedings of the 32nd Intersociety Energy Conversion Engineering Conference*, Vol. 2, pp. 1514-1518, Honolulu, HI.
- [6] Wirsch, P., and Thomas, S., 1996, "Performance Characteristics of a Stainless Steel/Ammonia Loop Heat Pipe," *AIAA Journal of Thermophysics and Heat Transfer*, Vol. 10, pp. 326-333.
- [7] Faghri, A., Gogineni, S., and Thomas, S., 1993, "Vapor Flow Analysis of an Axially Rotating Heat Pipe," *International Journal of Heat and Mass Transfer*, Vol. 36, pp. 2293-2303.
- [8] Faghri, A., and Thomas, S., 1989, "Performance Characteristics of a Concentric Annular Heat Pipe: Part I-Experimental Prediction and Analysis of the Capillary Limit," *ASME Journal of Heat Transfer*, Vol. 111, pp. 844-850.

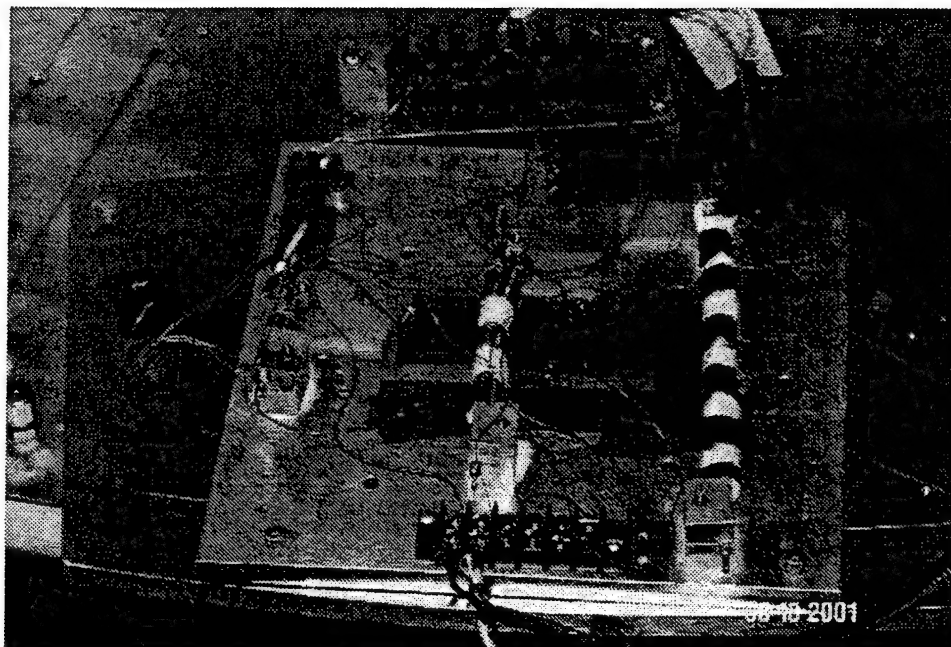


Figure 13: Close-up view of the heat pipe assembly mounted to the centrifuge table.

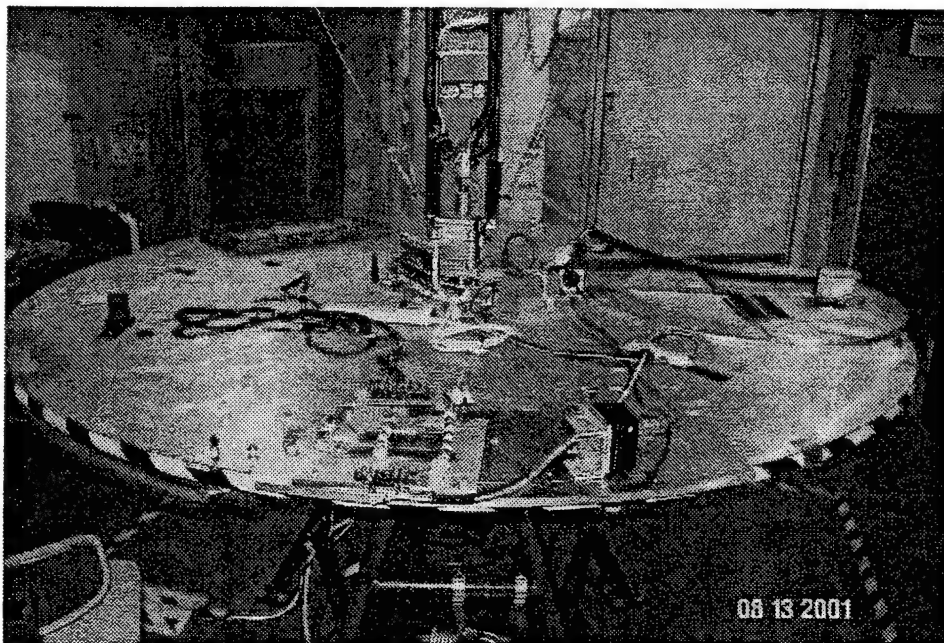
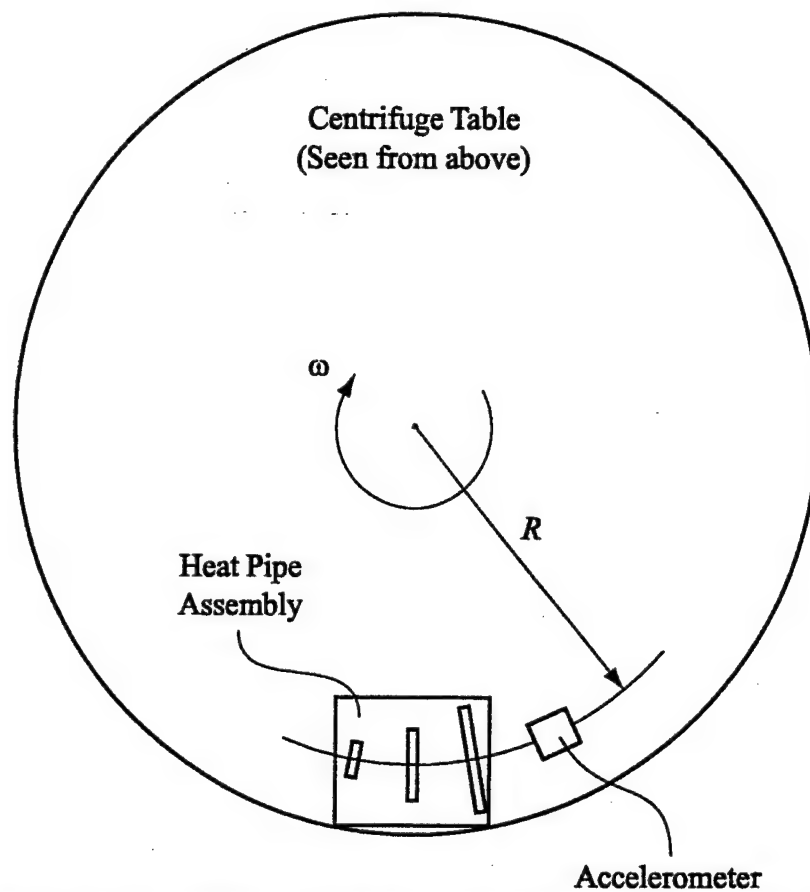


Figure 14: Placement of the heat pipe assembly on the centrifuge table ( $R = 44.5$  inches).

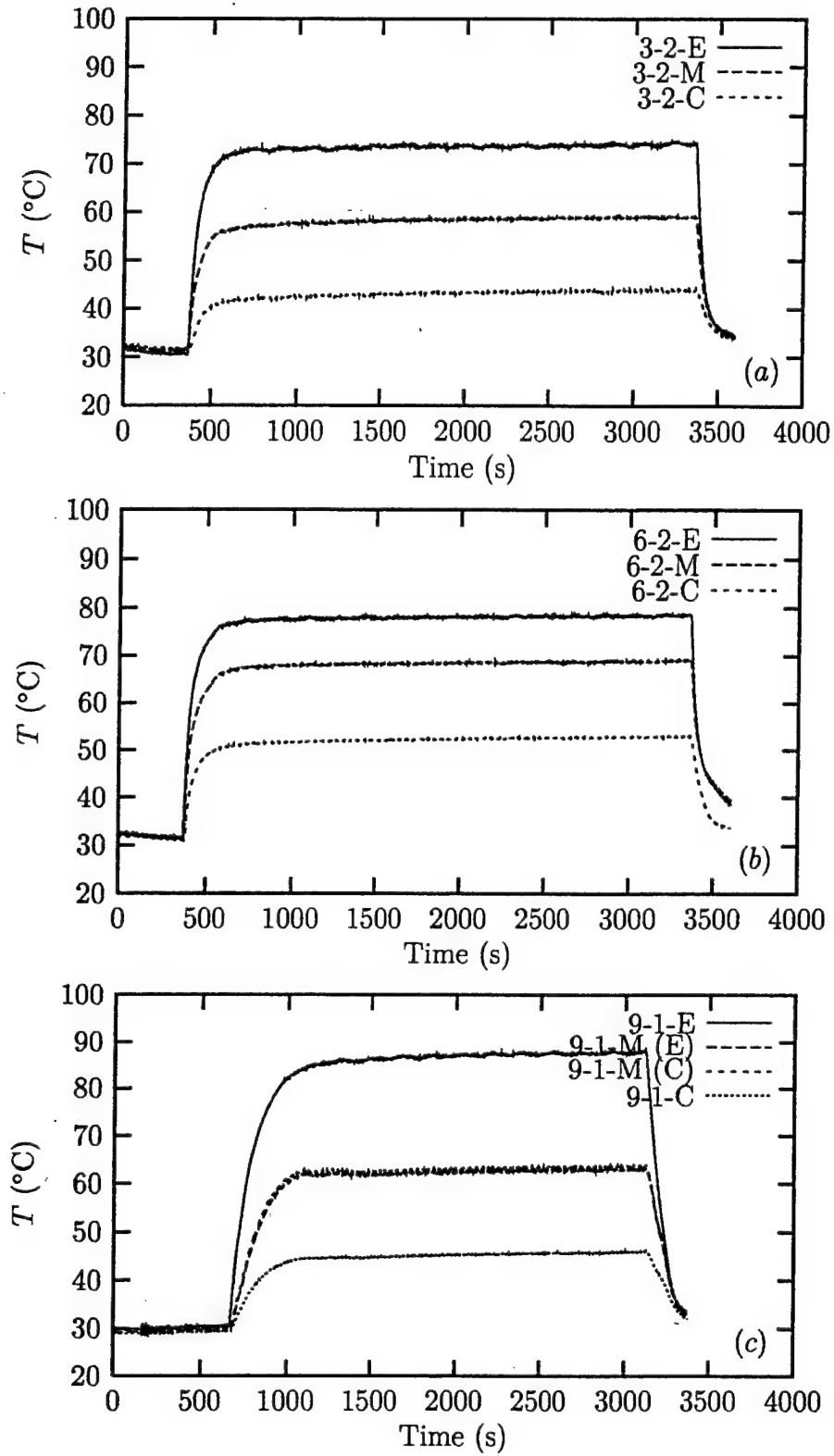


Figure 15: Typical start-up test results for  $a_r = 5.0$ -g: (a) 3IHP (RAY33); (b) 6IHP (RAY22); (c) 9IHP (RAY9).

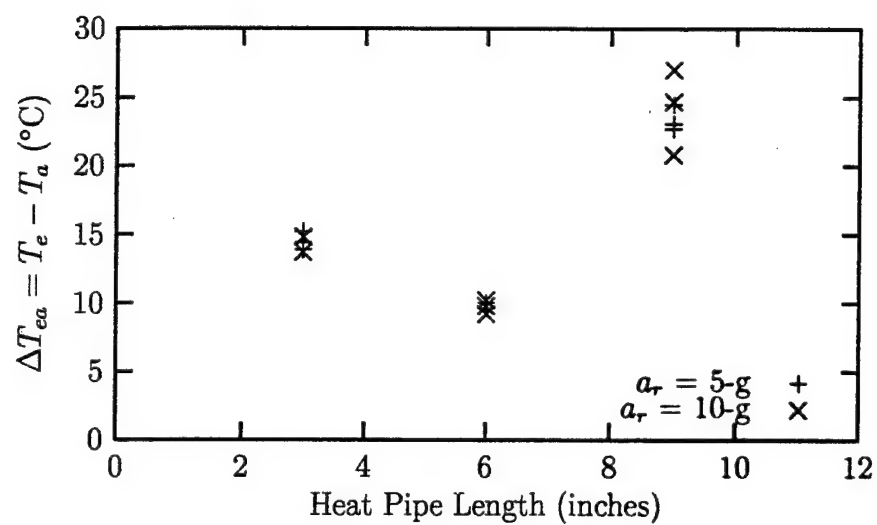


Figure 16: Temperature differences between the evaporator and adiabatic sections for the start-up tests.

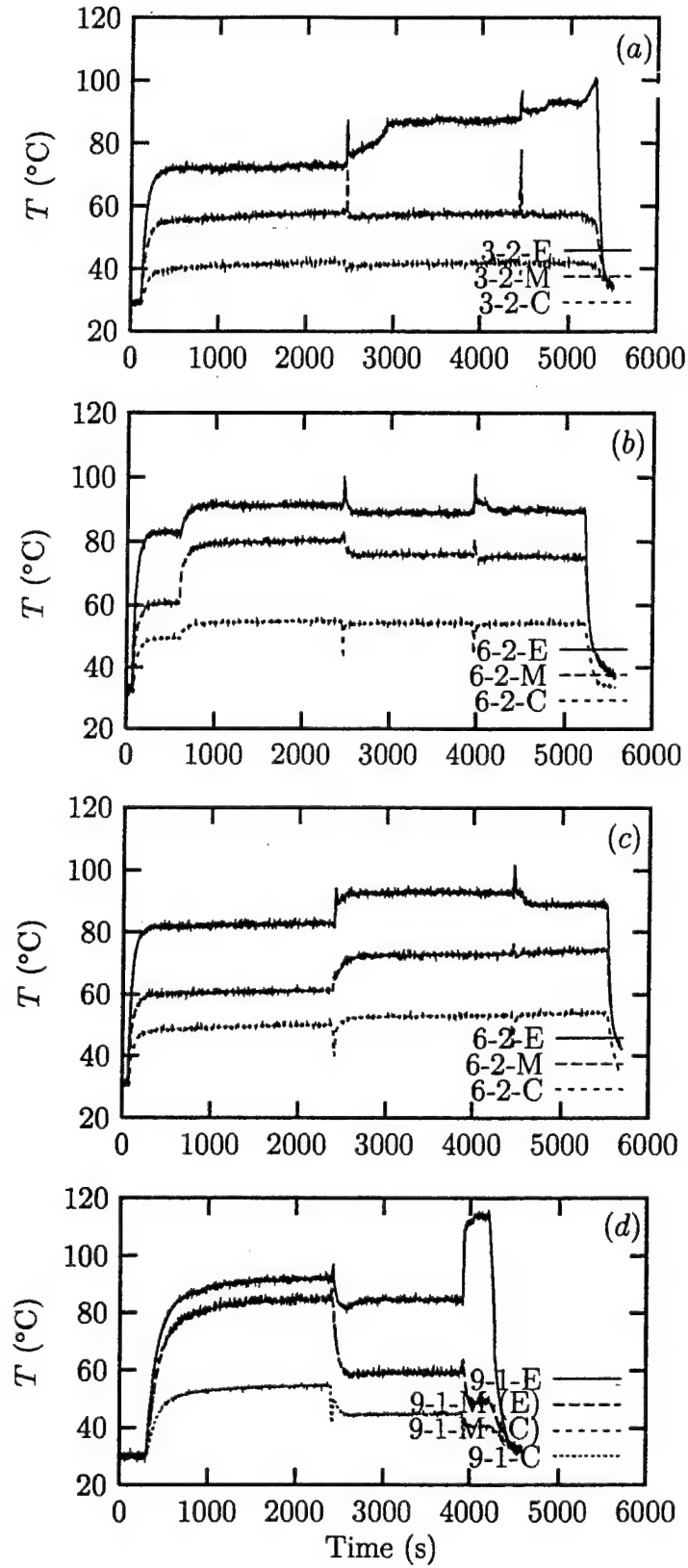


Figure 17: Typical burst test results for  $a_r = 5.0$ -g: (a) 3IHP (RAY28); (b) 6IHP (RAY16); (c) 6IHP (RAY17); (d) 9IHP (RAY2).

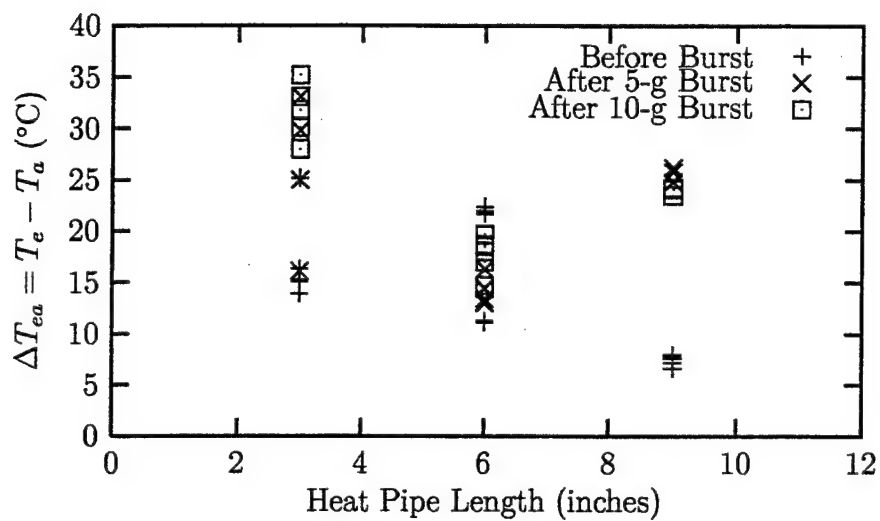


Figure 18: Temperature differences between the evaporator and adiabatic sections for the burst tests.

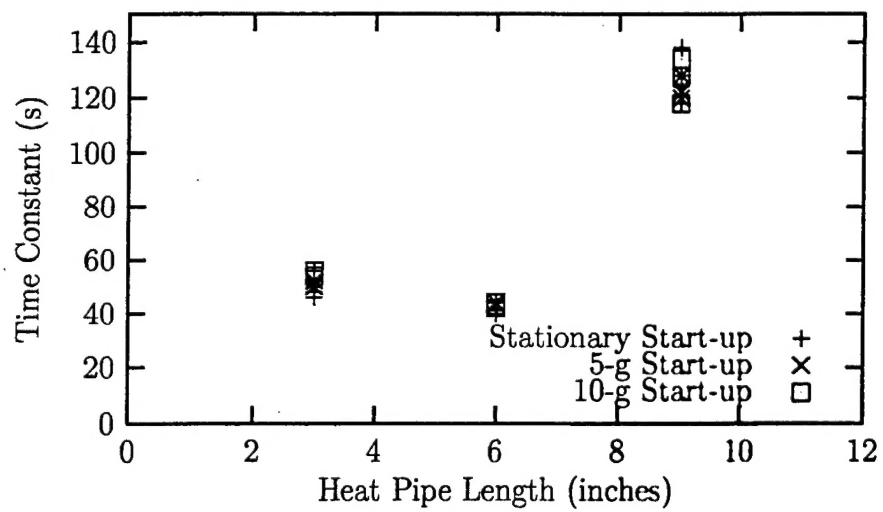


Figure 19: Start-up response characteristics.



Table 6: Temperature differences between the evaporator and adiabatic sections for the start-up tests (Fig. 16).

Heat Pipe Length (inches)	$\Delta T_{ea}$ ( $^{\circ}\text{C}$ )	
	$a_r = 5.0\text{-g}$	$a_r = 10.0\text{-g}$
3	14.4	13.7
3	15.2	13.7
3	13.9	14.8
6	9.6	9.8
6	10.0	9.2
6	9.6	10.2
9	22.7	20.8
9	23.1	24.7
9	24.5	27.0

Table 7: Temperature differences between the evaporator and adiabatic sections for the burst tests (Fig. 18).

Heat Pipe Length (inches)	$\Delta T_{ea}$ (°C)		
	Before Burst	After 5.0-g Burst	After 10.0-g Burst
3	25.2	25.0	x
3	16.3	16.1	x
3	15.1	29.8	x
3	15.2	x	35.2
3	13.9	x	31.8
3	15.3	x	30.1
3	x	29.8	x
3	x	33.1	x
3	x	x	33.1
3	x	x	28.0
6	11.3	13.0	x
6	21.7	14.4	x
6	11.1	13.1	x
6	21.9	x	19.7
6	22.0	x	18.5
6	22.4	x	18.7
6	x	13.4	x
6	x	16.3	x
6	x	14.5	x
6	x	x	14.7
6	x	x	18.0
6	x	x	17.0
9	6.6	24.8	x
9	7.2	25.8	x
9	7.6	26.2	x
9	7.7	x	24.2
9	8.0	x	23.5
9	7.9	x	24.1

Table 8: Start-up response characteristics (Fig. 19).

Heat Pipe Length (inches)	Start-Up Time Constant (s)		
	Stationary	$a_r = 5.0\text{-g}$	$a_r = 10.0\text{-g}$
3	x	50	x
3	52	52	x
3	50	52	x
3	56	x	54
3	48	x	54
3	46	x	56
6	x	44	x
6	44	44	x
6	40	44	x
6	42	x	42
6	40	x	44
6	42	x	44
9	x	122	x
9	138	120	x
9	124	128	x
9	128	x	134
9	118	x	118
9	118	x	128